CHARACTERIZATION OF SURFACE AND LAYERED FILMS

WITH CLUSTER SECONDARY ION MASS SPECTROMETRY

A Dissertation

by

ZHEN LI

Submitted to the Office of Graduate Studies of
Texas A&M University
in partial fulfillment of the requirements for the degree of

DOCTOR OF PHILOSOPHY

December 2007

Major Subject: Chemistry

CHARACTERIZATION OF SURFACE AND LAYERED FILMS

WITH CLUSTER SECONDARY ION MASS SPECTROMETRY

A Dissertation

by

ZHEN LI

Submitted to the Office of Graduate Studies of
Texas A&M University
in partial fulfillment of the requirements for the degree of

DOCTOR OF PHILOSOPHY

Approved by:

Chair of Committee,	Emile A. Schweikert
Committee Members,	D. Wayne Goodman
	Robert A. Kenefick
	Gyula Vigh
Head of Department,	David H. Russell

December 2007

Major Subject: Chemistry

ABSTRACT

Characterization of Surface and Layered Films with Cluster Secondary Ion Mass
Spectrometry. (December 2007)

Zhen Li, B.S., Beijing Normal University;

M.S., Beijing Normal University

Chair of Advisory Committee: Dr. Emile A. Schweikert

Cluster secondary ion mass spectrometry (SIMS) analyses of layer-by-layer thin films were performed to investigate the depth/volume of SI emission and accuracy of the SI signal. The thin-layered samples were assembled by alternate adsorption of polyethylenimine (PEI), polystyrene sulfonate (PSS), polydiallyldimethylammonium chloride (PDDA) and clay nanoparticles. The films have controlled 3-D structure to test the depth of secondary ion (SI) emission and evaluate planar homogeneity.

The SI emission depth is ~ 6-9 nm with 136 keV Au_{400}^{4+} (340 eV/atom) and 26 keV C_{60}^{+} (433 eV/atom) projectile impacts. The diameter of the SI emission area is ~ 15 nm by assuming a semispherical emission volume. The SI yields oscillate with the alternation of the compositions of the topmost layers, which was observed with small cluster projectiles ($CsICs^{+}$ and Au_3^{+}) as well as with the large cluster projectiles (C_{60}^{+} and Au_{400}^{4+}).

The SI signals of C^{-} and CH^{-} are enhanced in the presence of metal atoms in the expanding plume. Recoiled C_{60} projectile fragments (m/z=12, 13, 36) are observed in the SI mass spectra. Caution must be taken when monitoring the yields of such carbon cluster ions from organic surfaces because their yields don't reflect the true surface concentration.

The Au_{400}^{4+} projectile impacts produce abundant co-emission. The correlation coefficient between the co-emitted SIs can be used to evaluate the planar

homogeneity. The results show that the PSS layer is more uniform than the clay layers.

The effect of alkali metal ion implantation on the nature and abundance of SI emission was investigated on Cs^+ or Na^+ implanted glycine samples. The alkali metal implantation induces surface damage and decreases the glycine molecular ion yields. Glycine molecular ions and fragment ions (CN^-, CNO^-) are emitted from different depths and locations of the emission volume. The same implanted glycine sample analyzed with different cluster projectiles (Au_{400}^{4+} and C_{60}^+) shows different trends in the yields of molecular and fragment ions, which suggest a different mechanism of SI emission with different projectile impacts. The Na^+ beam induces more surface damage compared with the Cs^+ at equal impact energy.

DEDICATION

To

my parents, my wife and my grandparents,

who have been waiting for this moment for so long

ACKNOWLEDGMENTS

here. Graduate school is not easy, but hard work and good friends can make it through.

Finally, I would like to thank my parents and my wife for their never-ending love and support.

TABLE OF CONTENTS

LIST OF FIGURES

FIGURE   Page

LIST OF TABLES

CHAPTER I

INTRODUCTION

Secondary ion mass spectrometry (SIMS) is well recognized a sensitive surface analysis method [1]. It utilizes energetic charged particles (primary ions) to probe surfaces. Impacts from the high energy, high velocity projectiles cause desorption of surface species. Such secondary species include ions, electrons, neutrals, and photons (Figure 1-1). The charged particles, i.e., secondary ions (SI) and electrons can be extracted by an electric field, the SIs can be separated according to their mass to charge ratio and detected subsequently to obtain a mass spectrum. Depending on the properties of the primary ion used, the spectrum can be dominated with atomic and small fragment ions, which provide mostly isotopic/elemental information and hence little compositional information. In this study, we emphasis projectiles which cause abundant emission of molecular or "parent-like" SIs, which provide information characteristic of the surface. Rather surprisingly, the most efficient projectiles for this purpose are those depositing a high density of energy.

Desorption with keV and MeV Projectiles

SIMS operates in two different modes: dynamic SIMS and static SIMS. The major difference between these modes is the primary ion doses. In the dynamic SIMS, the primary ion dose is above 10^{13} ions/cm^2, sometimes as high as 10^{16-17} ions/cm^2 [2]. The high primary ion dose induces mixing at the beam/sample interface and removal (sputtering off) of surface materials. Due to the high dose, most of the SIs detected are atomic and small fragment ions. One advantage of the dynamic mode is that the overlayers can be removed at a steady rate by careful calibration of the sputtering rate. SIMS experiments conducted in this manner are depth profiling.

This dissertation follows the style and format of the International Journal of Mass Spectrometry.

Projectile

Atomic, polyatomic, cluster

Photons

Secondary electrons

Secondary ions

Neutrals
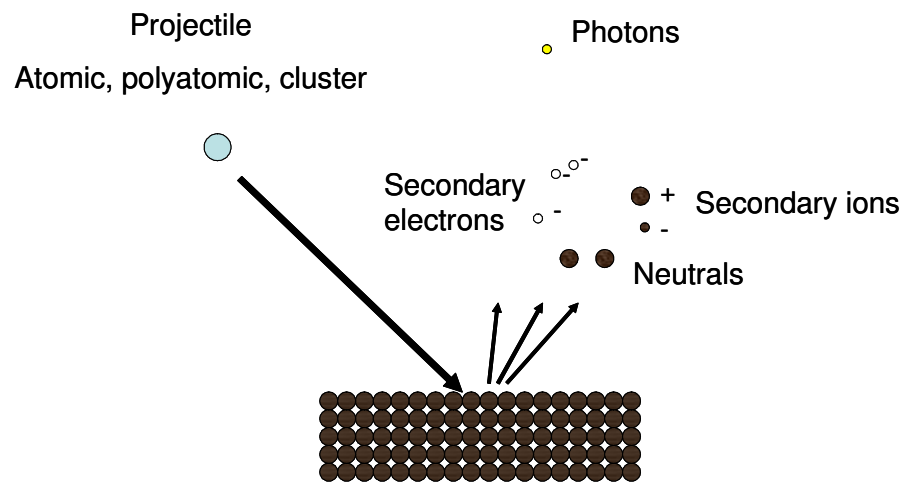
Figure 1-1 Schematic of SIMS sputtering process.

Static SIMS, in contrast to dynamic SIMS, involves smaller number of projectile impacts. The primary ion dose is below 10^{12} ions/cm^2. The volume probed by individual projectiles is a few nm in diameter and depth; thus, there is a low probability that an incoming projectile would impact a region that has been probed by other projectiles. Under this condition, only a small portion of the surface is probed by the projectiles with most of the surface remaining intact. Beam induced damage and atomization of the surface materials are minimized in static SIMS. More molecular or "parent-like" SIs can be detected in this mode. The major challenge for static SIMS is the low efficiency of the projectiles, i.e., SI yield. The SI yield is defined as the number of SIs detected per projectile impact. When using atomic projectiles, the SI yields range from one hundredth of a percent to a few percent. For example, when using 20 keV Cs$^+$ projectiles to impact a vapor deposited phenylalanine surface, the yield of phenylalanine molecular ion, (Phe-H)$^-$, is 0.37% [3].

The projectiles used for typical SIMS experiments have kinetic energies in the keV range. A technique akin to SIMS, called plasma desorption mass spectrometry (PDMS) was developed by Macfarlane and co-workers at Texas A&M University [4]. This method uses spontaneous fission fragments of radioactive isotopes (^{252}Cf) as projectiles. The kinetic energies of the projectiles are in the MeV range. The energetic fission fragments interact with the sample through electron stopping, instead of collision cascade with keV projectiles. PDMS was used for the desorption of organic and biological samples, especially before the introduction of cluster primary ions [5-12].

Cluster Primary Ions

The nature of the projectiles significantly influences the properties of the sputtering event and the type and yield of the SIs emitted [13]. As mentioned above, the molecular ion yield of phenylalanine with 20 keV Cs$^+$ projectile impacts is less

than 1%. Thus, a large number of projectiles are needed to obtain a statistically valid spectrum. In most cases, when using atomic projectiles, the spectrum is dominated with fragment ions that provide little surface-specific chemical information. Many researchers have reported that polyatomic projectiles can increase SI yields, especially from organic targets, and the emission of molecular or "parent-like" SIs [14].

Studies of the enhanced performance of polyatomic projectiles date back to the 1960s. Metallic surfaces of Ag, Cu were analyzed with KI^+, H_3^+, and other small cluster projectiles. It was observed that the sputtering yield of polyatomic projectiles is higher than the sum of the yield of individual constituent atoms impacting at the same velocity. This means that there is a collective or non-linear effect under polyatomic projectile impacts [15-19].

The performance of cluster projectiles can be assessed with an enhancement factor (ε), which can be defined as follows for a homomolecular projectile A_n with n constituent atoms:

$$\frac{Y_{An}(E)}{nY_A(E/n)} = \varepsilon$$

where $Y_{An}(E)$ is the yield of ions under cluster projectile (A_n) impacts with kinetic energy of E, and $Y_A(E/n)$ is the yield of ions under atomic projectile (A) impacts with impact energy of E/n. This means that both the cluster projectile and the atomic projectile have the same impact velocity. Researchers at Texas A&M University and the Institut de Physique Nucleaire at Orsay, France investigated cluster projectiles like $(CsI)_nCs$ (n=1 or 2), coronene ($C_{24}H_{12}$), and phenylalanine ($C_9H_{12}NO_2$) with 5-28 keV kinetic energy. Different types of targets, including phenylalanine, CsI, and Au were analyzed with these projectiles [20]. Enhancement factors up to 50 were observed in these experiments, which suggested a "supralinear" enhancement of the SI yields. Other researchers used a SF_6 beam to analyze Mylar, Teflon, and pharmaceutical compounds. SI yields increased by orders of magnitude under SF_6

cluster bombardments compared with atomic projectile impacts [21,22].

In 1991, the gold liquid metal ion source (Au-LMIS) was introduced for SIMS analysis. The LMIS can provide Au_n^{m+} cluster ions (n=1-5, m=1-2) and was used to measure the SI yield from a phenylalanine target. The "supralinear" effect was observed for all secondary ions from H^+ to molecular ions. The enhancement factor was larger for molecular ions than for atomic or fragment ions [23].

Boussofian-Baudin, et al. measured SI yield from a phenylalanine sample with 5-30 keV carbon cluster projectiles (coronene, C_{37}, C_{60}, and C_{70}). They showed similar enhancement effects as those from Au cluster impacts. They also showed that the phenylalanine yield was higher when using a more complex projectile (C_{60}) than with Au_4 at equal impact velocity, which suggests that the nature of the projectile could also affect the SI yield [24]. Other studies using cluster projectiles show increased SI yield with increased projectile atomic mass and complexity [25] and fragmentation-rearrangement of the secondary ions [26-28].

Vickerman's research group developed a C_{60} effusion ion source in 2003 [29,30]. The ion source can produce single or doubly charged C_{60} ions with kinetic energy up to 25 keV. C_{60} has many advantageous features as a cluster projectile. Because of its stable and symmetrical structure, C_{60} performs consistent impact geometry. In addition, it sublimes easily, which simplifies the design of the ion source. The mass of the constituent carbon atoms matches that of most organic, polymeric, and biological samples. This allows efficient collision energy transfer upon impact and facilitates the emission of organic molecules. The ion source was commercialized immediately upon introduction and now has been used widely for depth profiling [31-37] and imaging [38-40]. A similar C_{60} effusion ion source was independently designed and built at Texas A&M University and has been used for the analysis of organic materials [41].

Massive cluster projectiles with masses higher than 1000 amu were investigated by many research groups. Mahoney et al. produced massive glycerol projectiles with

more than 10^7 amu in mass and more than 100 charges; such projectiles showed reduced chemical noise and enhanced signal-to-noise ratio [42,43]. Charged proteins and peptides produced by electrospray ionization source were also investigated [44]. Massive Ar_n^+ cluster projectiles (n=1 - 5000) showed great enhancement in sputtering yield compared with atomic Ar projectiles [45].

In 2004, researchers at Orsay, France expanded the scope of the Au-LMIS [46]. The ion source now is able to produce large Au cluster projectile ions in addition to small clusters. These massive Au cluster projectiles contain 100-1000 Au atoms per projectile with 1 to 10 positive charges. One of the stable projectiles in this group is Au_{400}^{4+}. The Au_{400}^{4+} projectile showed great efficiency in the desorption of organic species. Multiple SIs can be detected within single impact/emission events and the yield of surface characteristic ions can reach more than 100% [47-51]. Such high efficiency makes it possible to probe the surface with only a few projectile impacts.

Topics of Interest with Cluster SIMS

Depth and Volume of SI Emission

Studies have been carried out regarding the mechanism of SI emission, i.e., interaction between the projectiles and the sample surface, removal of surface materials, and emission of SIs. Among these topics, one that bears significant analytical relevancy is the information depth and volume of the projectile. Molecular dynamic (MD) simulations of ~ 5 keV C_{60} impacts on various types of targets (water, graphite, diamond, benzene, etc.) show that the projectile shatters upon impact. The fragments of the projectile can penetrate ~ 5 nm into the target, and target materials can be removed from as deep as 10 nm [52-58]. Craters with a diameter in the 10-15 nm range are formed after impact. Computer simulation of Au_{402} cluster impacting a graphite surface shows a cylindrical crater with depth in the 10 nm range [59]. Such simulations provide visualization of the impact/emission process. However, only a small portion of the ejected surface materials are ionized and materials located at

different positions of the crater behave differently in terms of ionization and fragmentation. Experiments have been carried out to address the volume and depth of SI emission. Delcorte et al. investigated SI emission under atomic projectile impacts using a laminated polymer thin layer system [60]. Coupled with data from X-ray reflectivity, XPS, and AFM, they found a mean emission depth of 1.5 nm for the Si substrate under uniform polyelectrolyte thin layer films. Stapel et al. investigated SI emission from Langmuir-Blodgett (LB) films under atomic and small cluster projectile impacts [61]. SI signals from the Au substrate were observed even with 7 bilayers of LB films. Szakal et al. investigated the escape depth of Ag ions under amorphous water surface with C_{60} projectile impacts [55,62]. Still, there are few systematic investigations of the depth and volume of SI emission under cluster, especially massive cluster projectile impacts.

Ionization Efficiency

The negative SI yields increase when electropositive elements, especially alkali metals, like Cs^+, are used as primary ions [63-74]. The application of Cs^+ reduces the surface work function, and thus facilitates the emission of negative SIs. The degree of decrease in work function depends on the kinetic energy and intensity of the Cs^+ beam. The enhancement effect disappears and the work function returns to normal when the kinetic energy of the Cs^+ sputtering beam exceeds a certain threshold. The work function reaches a minimum and no longer decreases when the sample is subject to a Cs^+ beam for an extended period of time, which indicates saturation of the Cs surface concentration.

A highly focused Cs^+ beam with a spot size less than 50 nm was used to image biological samples [75-77]. The high intensity Cs^+ beam results in degradation and removal of the surface materials. The mass spectra are thus dominated with atomic and small fragment ions. A 3-D elemental map can be obtained by successive sputtering and imaging of the surface. The Cs^+ beam deposits Cs^+ ions into the target

and sputters SIs off the target. A steady state is reached when the deposition rate and sputtering rate of the Cs^+ reach equilibrium. Hence, the Cs surface concentration is almost constant under steady state, even though the absolute Cs^+ surface concentration is unknown.

Cation mass spectrometry (CMS) was developed to deposit reactive Cs atoms onto the sample surface. A neutral Cs beam generated from a Cs evaporator was used to deposit Cs *in situ*, while a 30 keV Ga^+ beam was used for SIMS analysis [78-81]. By tuning the relative intensities of these two beams, a constant Cs deposition rate and surface concentration can be achieved. CMS shows great improvement in detection sensitivity compared with using Cs^+ or Ga^+ beam alone.

Present Study

In this dissertation, two major topics are investigated and discussed: a) the depth and volume of SI emission with cluster projectile impacts, and b) the effect of *ex situ* alkali metal ion implantation on SI emission with cluster projectile impacts.

The first topic was investigated using four sets of specially designed layer-by-layer thin films. Primary ions used to analyze these thin layer films included $CsICs^+$, Au_3^+, ^{252}Cf fission fragments, C_{60}^+, and Au_{400}^{4+}. The experiments were conducted under event-by-event bombardment/detection mode, where a sequence of individual projectiles each strikes an unperturbed area of the target, i.e., in a manner analogous to how MD simulations are carried out. SIs emitted from the thin layer films with varying thicknesses were monitored and compared to evaluate the volume and depth of SI emission. The capabilities of cluster projectiles to probe planar homogeneity and depth integrity were also demonstrated.

Cluster projectiles show enhanced SI signals compared with equal velocity monatomic projectiles. Such enhancement can be due to enhanced sputter yield (where more surface materials are removed from each impact), or enhanced ionization probability, or a combination of both. The second topic of this dissertation

investigated the effect of alkali metal implantation on ionization probability. Vapor-deposited amino acid samples were analyzed with C_{60}^+ and Au_{400}^{4+} projectiles before and after subjecting the samples to alkali metal ion beams (Cs^+ and Na^+) with varying kinetic energies and intensities. SI signals from the molecular and fragment ions of the amino acid samples were monitored and compared before and after implantation.

CHAPTER II

INSTRUMENTATION AND SAMPLE PREPARATION

The following chapter describes setups of four time-of-flight (TOF) SIMS instruments, which were used for the studies described in Chapters III to VI, as well as the procedures of sample preparation.

^{252}Cf Fission Fragment-based Mass Spectrometers

^{252}Cf fission fragment-based mass spectrometers were used to analyze samples in Chapter III. There are two different setups based on the ^{252}Cf source. The first setup uses ^{252}Cf fission fragments directly as projectiles. The second setup uses primary ions desorbed by the ^{252}Cf fission fragments impacting a CsI foil.

In the first setup (Figure 2-1), fission fragments from the ^{252}Cf radioactive decay are used directly as primary ions. ^{252}Cf radionuclide has a half-life of 2.645 years. 3.1% of its radioactive decays are spontaneous fissions, while the rest are α-decays. The fission fragments are emitted at ~ 180° from each other with a distribution of mass (95-160 amu) and charge states (18-22). The kinetic energy carried by the fission fragments is roughly 1 MeV per amu [82,83]. Among these fission fragments, only a small portion (~ 6%) can pass through the 1/4-inch collimator in which the source is housed. One of the two complementary fission fragments impacts the sample target as the primary projectile. The other fission fragment passes through a negatively biased conversion foil. The conversion foil is an aluminized Mylar foil vapor deposited with CsI. The impact of the fission fragment into the conversion foil causes electron emissions from the CsI. The electrons are accelerated by the negative bias towards the start (electron) detector. The conversion foil reduces the number of false starts caused by α-particle impacts, which also desorb secondary electrons but with fewer amounts compared with fission fragment impacts. By setting a certain

threshold at the electron detector, only the electron signals corresponding to the fission fragment impacts (with higher intensity) are recorded. SIs desorbed by the fission fragment impacts are extracted by a high voltage bias between the sample target (± 8 keV, depending on the polarity of SIs interested) and the grounded extraction grid. After separation through a field-free drift region, the SIs are detected by the stop detector, which is housed at the end of the vertically mounted flight tube (total flight length 55.6 cm). The ^{252}Cf source (Isotope Products, Burbank, CA) is placed at an equal distance (3 cm) between the target and the conversion foil. The axis of the source collimator is 30° from the sample surface normal (the impact angle of the fission fragment projectiles is thus 30°), the total sample surface exposed to fission fragment impacts is ~ 2 cm^2. We assume the time needed for electrons to fly from the conversion foil to the start detector is negligible, and then the start detector detects electrons from the conversion foil at the same time as the other fission fragment impacts the target. The time difference between the start and stop detector is recorded by a high-resolution timing device and can be converted to mass with proper mass calibration (see TOF Mass Spectrometer section in this Chapter for a detailed explanation). A mass spectrum is obtained in this manner by accumulating hundreds of thousands of such impact events.

The PDMS instrument is housed in a high vacuum chamber maintained by a 500L/s Edwards Speedvac B04 oil diffusion pump (Edwards Inc. Wilmington, MA). The diffusion pump is cooled with 15 ℃ chilled water and backed by an Edwards E2M28 28 cubic feet/min (CFM) two-stage mechanical roughing pump. The ultimate pressure of the system is ~ 5×10^{-7} torr. Sample introduction is achieved through a vacuum interlock (rotary linear direct motion feedthrough). The feedthrough is housed in the sample introduction chamber that can be differentially pumped to ~ 10^{-3} torr. The sample is mounted at the end of the feedthrough. A gate valve is placed between the main vacuum chamber and the sample introduction chamber. The valve is closed when a new sample is loaded into the introduction chamber. After the
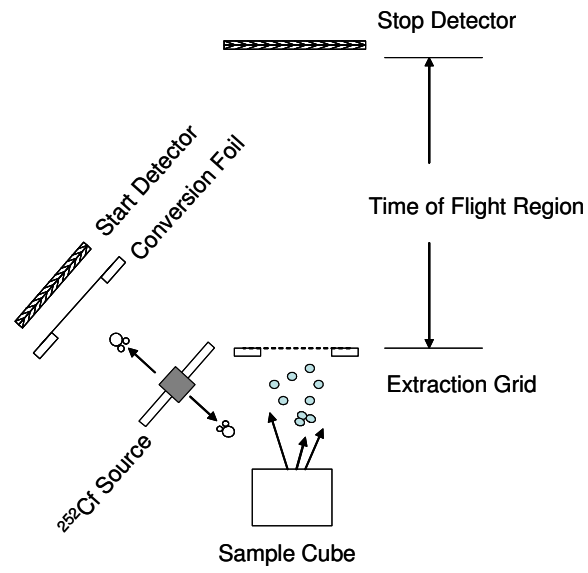
Figure 2-1 Schematic of the PDMS mass spectrometer.

introduction chamber is closed, it is pumped down by an auxiliary mechanical pump to ~ 10^{-3} torr. The gate valve is then opened to introduce the sample into the main chamber. The vacuum interlock reduces the amount of air leaked into the main chamber during sample introduction. After sample introduction, the feedthrough is retreated back to the introduction chamber and the gate valve is closed.

The second fission fragment-based SIMS instrument uses "transmission" primary ion geometry to produce $(CsI)_nCs^+$ (n=0 to 2) cluster primary ions (Figure 2-2). In this setup, the ^{252}Cf source is placed between two CsI conversion foils. One of the foils is negatively biased and acts as an electron conversion foil as in the PDMS for the start detector. The other foil is positively biased, when the energetic fission fragments pass through the foil from the backside, $(CsI)_nCs^+$ cluster ions are formed and accelerated through a set of extraction grids (also positively biased, but at lower potential) towards ground. The extracted $(CsI)_nCs^+$ cluster ions are used as primary ions to impact sample surfaces. The total kinetic energy of the primary ion is 13 keV. When the primary projectiles approach the target, they are accelerated again by a negative bias on the target (6 keV), which results in a total impact energy of 19 keV for the $(Cs))_nCs^+$ cluster projectiles. Since the target is negatively biased, this setup can only be used for the detection of negative SIs, and it loses the flexibility of the PDMS instrument, which can detect SIs of both polarities. The key feature of this arrangement is the capability of providing a wide selection of cluster projectiles. Indeed, many other compounds may be used in place of CsI to generate cluster projectiles [3].

Secondary ions and electrons generated by the primary projectile impacts are extracted by the target bias. A weak magnet is placed in front of the SI extraction grid. Electrons are steered away from the straight trajectory due to their light weight; while the weak magnet field has little effect on the straight flight trajectory of most ions. The steered electrons are detected by the secondary electron detector (stop 1). The secondary ions fly straight down the ~ 48 cm flight tube and are detected by the
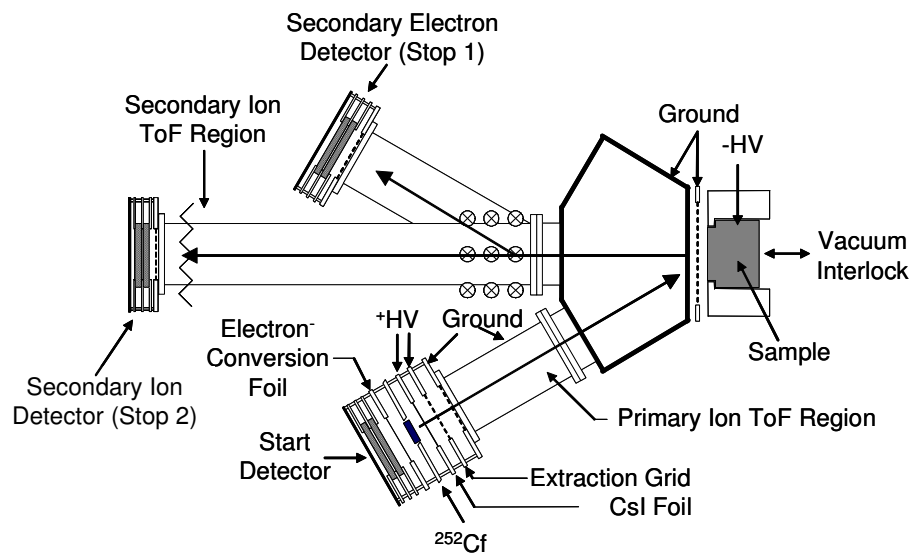
Figure 2-2 Schematic of ^{252}Cf $(CsI)_n Cs^+$ cluster ion mass spectrometer.

secondary ion detector (stop 2). The time difference between the primary ion impact and the detection of secondary electrons is negligible due to the light weight of the electrons and the high target bias (6 keV). Thus, the time when the secondary electrons are detected can be regarded as the time of the primary ion impact. The start detector and the stop 1 detector formed the first TOF stage, i.e., primary ion TOF. The primary ion TOF can be used to distinguish different types of primary ions generated by the fission fragment impacts, i.e., Cs^+, $CsICs^+$, and $(CsI)_2Cs^+$. The second TOF stage is between the stop 1 and 2 detectors. A SI mass spectrum is obtained by recording the flight time between stop 1 and stop 2 detectors and accumulating hundreds of thousands of such events. However, such SI mass spectrum contains SIs emitted from impacts of all types of primary ions generated by the fission fragment impacts. In order to differentiate SIs emitted from different types of primary ion impacts, the data acquisition software is designed in such a manner that the stop 2 detector is open only at certain timeframes. Such timeframes are called "windows," and are set by checking the primary ion TOF spectrum. For example, by putting a window around the primary ion TOF peak of $CsICs^+$, a SI mass spectrum corresponding only to the $CsICs^+$ cluster projectile impacts can be obtained, while SIs originated from other projectile impacts are discarded by the software. Although the software is set for acquiring only SIs originated from certain type of primary ion impacts, the SI mass spectrum is still convoluted due to variations in impact angle and a large impact area (~ 2 cm^2), which produce aberrations in the arrival time of the primary ions. Again, a software function is used to compensate for the time aberration. The software shifts the arrival time of all primary ions in a selected window to the very beginning of the window. Secondary ions corresponding to the specific primary ion impacts are also shifted with an equal amount of time. An example of the shifted mass spectrum is shown in Chapter III (Figure 3-1).

The CsI cluster TOF-SIMS instrument is housed in a vacuum chamber similar to the PDMS system with similar pumping and sample introduction mechanism, but the

flight tube is mounted horizontally instead of vertically in the PDMS.

The major advantages of the ^{252}Cf-based SIMS instruments are the stable performance of the ^{252}Cf source and the ease of operation. However, since its operation is dependent on the radionuclide decay, the activity of the source is the bottleneck of the instruments. With an initial activity at 50 μCi in 1992 and 2.6 years of half life, the rate of decay is slow after 6 half-lives. It may take as long as 24 hours to obtain a mass spectrum. Thus, instruments equipped with other types of cluster ion sources are used to increase the efficiency as well as the duty cycle.

C$_{60}$ Effusion Source Mass Spectrometer

The C$_{60}$ effusion source mass spectrometer (Figure 2-3) was used to conduct experiments described in Chapters V and VI. The mass spectrometer contains two major components: the C$_{60}$ ion source and the TOF mass spectrometer. The design of the C$_{60}$ effusion ion source follows that from Vickerman's group [29,30]. C$_{60}$ powder (Sigma-Aldrich, Milwaukee, WI) is placed in a copper reservoir and heated in vacuum to its sublimation temperature ($\sim$ 450 ℃). The C$_{60}$ vapor effuses through the orifice of the reservoir into the ionization chamber (Figure 2-4). The cylindrical electrode in the ionization chamber is made of stainless steel tube, with most of the surface area (80%) replaced with a 0.01-inch diameter tungsten wire grid. Another tungsten wire (electron ionization filament) is wrapped around the electrode with $\sim$ 5 mm distance from the electrode. The wire is heated to white hot and there is a 30-100 V potential gradient between the filament and the cylindrical electrode. Thermal electrons generated by the ionization filament are accelerated towards the cylindrical electrode. The thermal electrons penetrate through the open space of the electrode, impact the C$_{60}$ vapor inside the electrode, and cause electron impact ionization of the C$_{60}$. The ionization process produces a wide variety of cations ranging from H$^+$ to C$_{60}^+$.

The cations produced in the effusion source are extracted by a voltage gradient
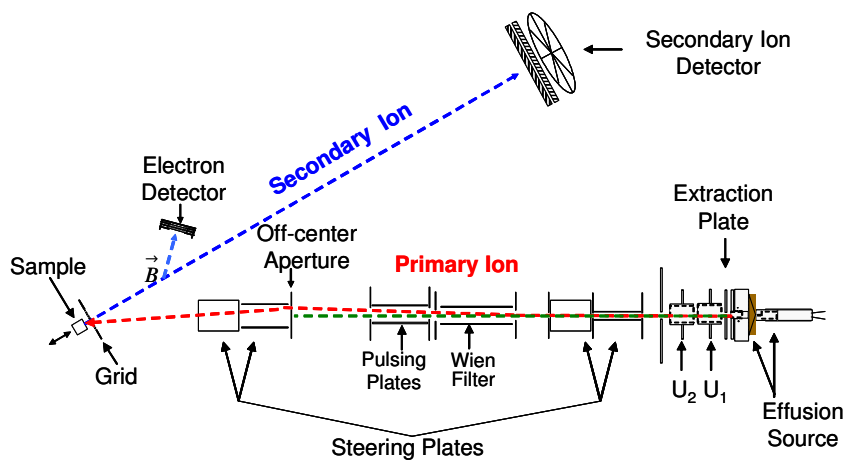
Figure 2-3 Schematic of the C$_{60}$ effusion source time-of-flight mass spectrometer.
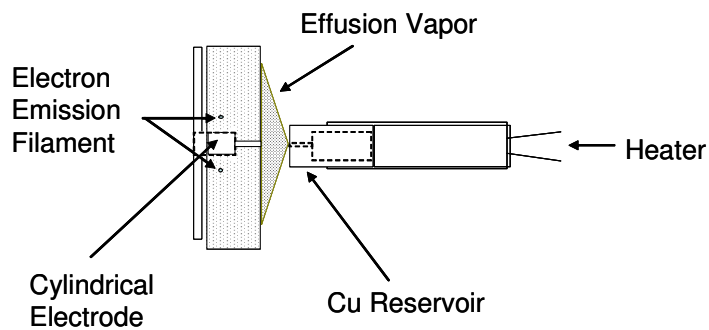
Figure 2-4 Schematic of the effusion source assembly.

between the cylindrical electrode and the extraction plate. The ions are accelerated toward ground through a set of electrostatic lens, which focus the extracted beam. The mixed beam then passes through a set of steering plates, where the trajectory of the beam is fine-tuned so that the beam can enter the Wien filter with a proper trajectory. The Wien filter selects ions with the proper mass to charge ratio and steers them towards the off-center aperture.

A Wien filter consists of an electric field and a magnetic field, which are perpendicular to each other. It is used to separate ions of different mass to charge ratio. Mass selection is based on ion velocity. The velocity of ions passing straight through the filter is as follows:

$$v = (10^8 \frac{V_d}{dB})$$
<div align="right">Eq. 3-1</div>

where v is the velocity of the ion in cm per second, V_d is the potential applied to the electric plates in volts, d is the distance between the electric plates (cm), and B is the strength of the magnetic field in Gauss. Combining Eq. 3-1 with the relationship between the kinetic energy and the velocity of ions yields the following equation (Eq. 3-2), which specifies the relationship between the potential on the Wien filter electric plate and ions of given mass and kinetic energy that can pass straight through the Wien filter:

$$V_d = K_1 \sqrt{\frac{E_K}{m}}$$
<div align="right">Eq. 3-2</div>

where K_1 is a constant that incorporates parameters of the Wien filter (magnetic field strength and electric plate distance), E_K is the kinetic energy of the ion, and m is the mass of the ion [84]. Thus, for a given Wien filter to separate ions with identical kinetic energy, the only variable parameter is the potential on the electric plates. By biasing the Wien filter plates at a certain voltage, only ions with a certain mass-to-charge ratio can pass through it, with other ions colliding with the plates.

After ionization, some ions undergo metastable decay. This process produces high energy/velocity neutrals, which are not affected by the electric or magnetic field

in the steering plates and Wien filter. These neutrals present several problems. First, when the high energy neutrals impact the sample, they also cause secondary emissions, like primary ions. Second, the masses of the neutrals are unknown because the Wien filter can not perform mass selection on neutrals. Third, the kinetic energy of the neutrals is unknown because the neutrals can be formed before ions obtain full kinetic energy or the kinetic energy can be lost during the decay/dissociation process. To overcome these problems, the neutrals must be removed from the primary ion beam prior to impact. This is achieved by placing an off-center aperture at the exit of the Wien filter. The neutrals, which are not affected by the electric field of the Wien filter, move in a straight trajectory and collide into the solid side wall of the off-center aperture. Ions are steered slightly by the Wien filter, so that they can pass through the opening of the off-center aperture and impact the sample surface. Prior to impact, the primary ion beam is steered by a second set of steering plates to align the SIs emitted to the center of the 8-anode detector. The positively charged primary ions are accelerated right in front of the target by the SI extraction bias (-10 keV). Secondary electrons emitted are steered slightly by a weak magnet field and detected by the electron (start) detector. While secondary ions are detected by the 8-anode stop detector. A mass spectrum is obtained by recording the flight time of the SIs along the 92.9 cm flight tube and accumulating ~ 1 million of such events.

Verification of the primary ion beam is achieved by rastering the mass selected primary ion beam across the 1 mm off-center aperture with a set of pulsing plates. Logic pulse at 5 kHz, ± 1 V is supplied by a Hewlett-Packard 8005B pulse generator. The pulse is routed to a high frequency MOSFET switch powered by two high voltage power supplies (supplying ~ 350 V dc power). Two outputs from the MOSFET switch are connected to the pulsing plates through vacuum feedthrough. One of the plates is grounded while the other one alternates between positive and negative high potential. The primary ions are swept across the off-center aperture by
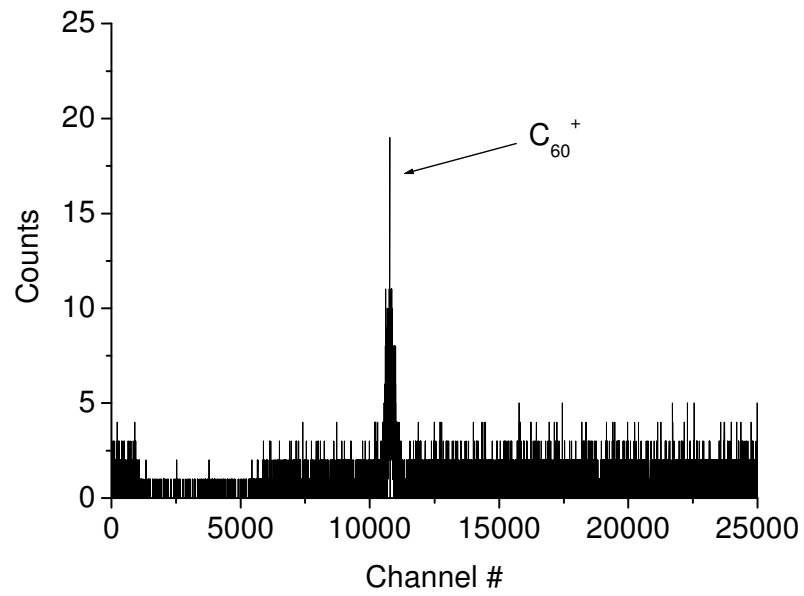
Figure 2-5 Mass selected 16 keV C_{60}^{+} primary ion TOF spectrum.

the alternating potential. Only a few of them have the proper trajectory to pass through the aperture, impact the target, and induce secondary electron/ion emission. A primary ion TOF spectrum is obtained by correlating the start of the pulsing with the detection of secondary electrons at the electron detector (Figure 2-5). Once the identity of the mass selected primary ion beam is determined, the pulsing electronics are turned off for the duration of the data acquisition. The flux of the C_{60}^+ primary ion beam can be controlled by adjusting the temperature and potential of the electron ionization filament. During experiments, the C_{60} flux is controlled so that 2000 to 3000 start signals are registered at the electron (start) detector every second. This flux can guarantee event-by-event mode bombardment/detection. The total area exposed to the C_{60}^+ beam is ~ 1 mm^2.

The C_{60} effusion source is housed in a cubic stainless steel chamber. Vacuum of the chamber is maintained by a Pfeiffer 60 L/s turbomolecular pump (Pfeiffer Vacuum, Nashua, NH), which is backed by an 8 CFM Varian two-stage rotary vane mechanical pump (Varian Inc. Palo Alto, CA). The ultimate pressure of the chamber is 1×10^{-6} torr at idle and 5×10^{-6} torr when the effusion source is under full operational condition. C_{60} vapor from the source contaminates roughing pump oil and the pump oil needs to be drained and replaced every two months under heavy working condition. C_{60} also deposits on the electrostatic lens and thermo/electric insulation materials, and the excessive deposition of the residues causes sparking between the high voltage components and the insulators, which ultimately leads to unstable performance of the ion source. The thermal electron emission tungsten filament deteriorates with usage as well. Signs of an aged filament include: high heating current on the filament and high electron impact voltage (>120 V) to maintain a steady C_{60} beam. It is advisable to clean the chamber and the source assembly, as well as to replace the tungsten filament at the same time. An improperly installed tungsten filament can also show symptoms similar to an aged filament. A new filament must be installed instead of correcting the malfunctioning one.

Gold Liquid Metal Ion Source Mass Spectrometer

A gold liquid metal ion source, Au-LIMS, TOF-SIMS instrument was used to analyze samples mentioned in Chapters III to VI (Figure 2-6). A detailed description of the instrument is available elsewhere [85,86].

In brief, Au-Si eutectic (97% gold, 3% silicon, Academy Precision Metals, Albuquerque, NM) is filled into a tightly wound tungsten wire coil reservoir. Another straight piece of tungsten wire (the needle) passes through the center of the reservoir and its tip extends 1.3 mm above the reservoir. A wide variety of Au_n^{m+} ($1 \leq n \leq 1000$, $1 \leq m \leq 10$) cluster ions can be produced by heating the Au-Si eutectic to its melting temperature and applying a high voltage between the needle and an extraction electrode (placed 1 mm from the tip of the needle). The extracted Au ion beam mixture (with ~ 20 keV kinetic energy) is focused by a series of electrostatic lenses (Einzel lens) and introduced into a Wien filter. By setting different values at the deflection plates of the Wien filter, only Au cluster ions with a certain mass-to-charge ratio can be selected to pass through the exit orifice of the Wien filter. Individual Au clusters can be selected by the Wien filter up to Au_9^+. For clusters with more than 9 atoms, the Wien filter can only select ions within a specific mass to charge range. For example, the massive Au cluster (Au_{400}^{4+}) is a group of Au cluster ions with an average of 400 gold atoms and 4 positive charges per projectile. After mass selection, the Au cluster projectiles are introduced into a high voltage pulsing system, where the projectiles are rastered against a 400 μm aperture. The pulsing system reduces the flux of the primary ion beam to guarantee event-by-event mode bombardment and detection. The pulsed beam then passes through a set of steering plates, where the beam can be steered both vertically and horizontally to align the SIs emitted to the center of the secondary ion detector. The Au clusters are accelerated towards the negatively biased target (6-9 keV) before they impact the target surface. Secondary electrons generated from the impacts are steered away by a weak magnet and serve as the start signal for the SI TOF. SIs emitted from the impacts are detected at the end
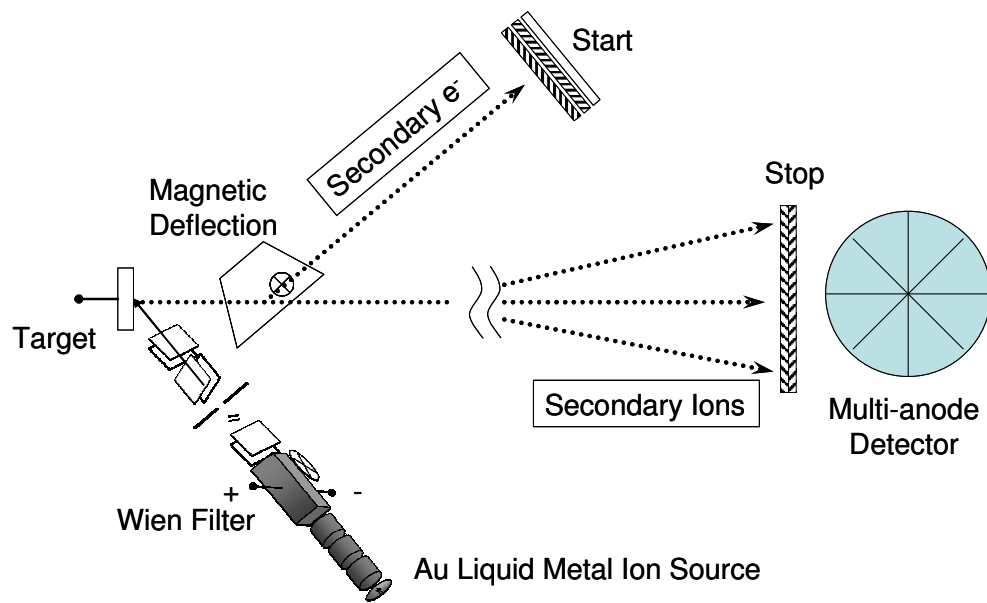
Figure 2-6 Schematic of the Au-LIMS TOF-SIMS system.
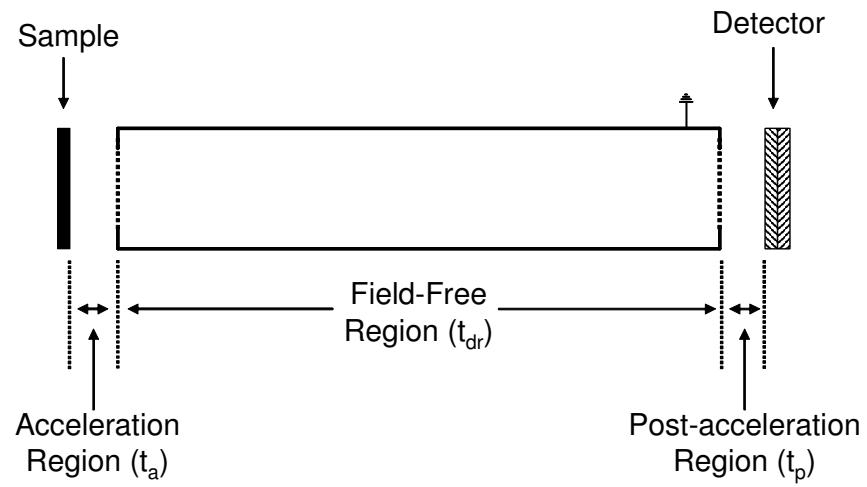
Figure 2-7 Schematic of time-of-flight.

of the 88.3 cm flight tube with an 8-anode detector. The total area subjected to Au cluster projectile impacts is ~ 1 mm^2.

TOF Mass Spectrometer

The Au-LMIS and C_{60} cluster TOF-SIMS systems have similar designs in the secondary ion mass spectrometer leg. Both have an electron (start) detector and an 8-anode secondary ion (stop) detector. The SI leg is separated from the primary ion leg by a gate valve, which acts as a barrier to block the primary ion beam from impacting the target between data acquisition. The gate valve also helps maintain the vacuum in one side of the instruments when the other side is opened to ambient pressure for service. The mass spectrometer chamber is evacuated by an Edwards 160/700M oil diffusion pump backed by an 11 CFM rotary vane mechanical pump. The ultimate pressure of the chambers is maintained at ~ 10^{-7} torr. Sample introduction is achieved with the direct motion feedthrough mentioned in the ^{252}Cf fission fragment instruments. The sample cubes (stainless steel or brass, 7/8-inch in each dimension) are secured in a Teflon sample holder and biased with negative high voltage. A grounded 90% transmission grid (Precision Eforming, Cortland, NY) is placed 0.375 inches away from the sample cube surface. The biased target and the grounded grid form the extraction field for the SIs and electrons. The flight tube is horizontally mounted with an 8-anode detector mounted at the end. The 90% transmission grid results in a 90% transmission efficiency for the mass spectrometers described here.

Secondary ions proceed through three regions between their formation and detection: acceleration region, drift (field-free) region, and post-acceleration (deceleration) region [87]. The total flight time of an ion is a summation of the flight time through the above three regions (Figure 2-7):

$$t_{tot} = t_a + t_{dr} + t_p \qquad\qquad \text{Eq. 3-3}$$

where t_{tot} is the total flight time, t_a is the acceleration time, t_{dr} is the flight time in the

drift region, and t_p is the time spent in the post-acceleration region.

The flight time in these three regions can be calculated as follows:

$$t_a = (2md_a^2 / zV_a)^{0.5}$$
Eq. 3-4

$$t_{dr} = (md_{dr}^2 / 2zV_a)^{0.5}$$
Eq. 3-5

$$t_p = (d_p^2 (2m)^{0.5} [(V_a + V_p)^{0.5} \pm V_a^{0.5}]) / z^{0.5} V_p$$
Eq. 3-6

$$t_{tot} = (2md_a^2 / zV_a)^{0.5} + (md_{dr}^2 / 2zV_a)^{0.5} + (d_p^2 (2m)^{0.5} [(V_a + V_p)^{0.5} \pm V_a^{0.5}]) / z^{0.5} V_p$$
Eq. 3-7

where V_a is the high voltage bias applied to the target, d_a is the distance between the

target and the grounded grid, d_{dr} is the length of the drift region, m is the mass of the

secondary ion, and z is the charge state of the ion. When the instrument is set at

working condition, all the values in Eq. 3-7 are set except for the mass and charge

state of the ions. Thus, the total flight time of ions with certain mass to charge can be

calculated from the above formula.

In practice, mass calibration is obtained using Eq. 3-8:

$$(m / z) = [(t_{tot} - C_2) / C_1]^2$$
Eq. 3-8

where C_1 is a constant determined by the target bias and the flight length, and C_2 is

determined by the response speed of the timing electronics [88]. The values of these

two constants can be obtained by filling the equation with two ions of known mass to

charge ratio (e.g., H⁻ and C_2H⁻, etc.). Resolution of the mass spectrometer is defined

as m/Δm (Eq. 3-9); typical mass resolutions of the mass spectrometers used here are

~ 500-1000.

$$\frac{m}{\Delta m} = \frac{t}{2\Delta t}$$
Eq. 3-9

Detectors and Detection Electronics

Secondary ions and electrons are detected by microchannel plate (MCP) detectors.

The long life non-imaging grade MCPs were supplied by Burle Electro-Optics

(Sturbridge, MA). Detectors used on the single anode detectors are 30 mm in

diameter with 25 mm active area. Detectors used on the 8-anode detectors are 50 mm in diameter with 40 mm active area. The MCPs are made of lead-doped glasses. The diameter of each channel is 10 μm, and the thickness of the sidewall is 1μm. A detector plate is obtained by fusing millions of such small channels together. The channels are assembled at 12° from surface normal. During operation, a high voltage (~ 1 kV) is applied across the plate. Any impacts from objects with momentum (ions, electrons, or neutrals) lead to electron cascade in the MCP; a gain of 10^3 can be achieved through each plate. By stacking two MCPs together in a chevron configuration, a total gain of 10^6 can be achieved. The detection efficiency of the MCPs is velocity dependent, that is, under the same kinetic energy, lower mass ions have higher detection efficiency than higher mass ions [89,90]. A collection anode is placed at the exit of the MCP to collect the electron cascade cloud. The difference between the single anode and the 8-anode detector is the design of the collection anode. For a single anode detector, a single piece of brass plate is used as the collector, while for the 8-anode detector, an 8-segment collector made of copper-plated circuit board is used (Figure 2-8) [86]. The advantage of the 8-anode detector is the capability of detecting simultaneous impacts of SIs with the same m/z. The active surface area of the 8-anode detector is 93% of the total surface. This value coupled with the detection efficiency of the MCPs (~ 50%) and the transmission of the TOF mass spectrometer (90%) result in a final detection efficiency of ~ 40% for SIs in the mass range 100-200.

The TOF-SIMS instruments mentioned in this dissertation use the pulse counting mechanism to record SI striking the detector. When two SIs of the same m/z impact the detector at the same time, the collection anode gives out a single pulse with higher amplitude compared with a single SI strike. The pulse counting electronics can only recognize occurrence of the pulse regardless of its intensity. Thus, regardless of a single strike or simultaneous double or multiple strikes, the electronics can only recognize one pulse and record it as a single SI in the mass
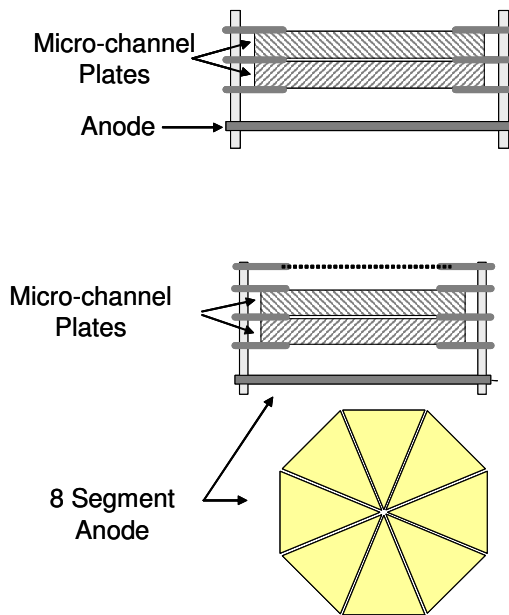
Figure 2-8 Schematic of the microchannel plate detector assemblies.

spectrum. Under such situations, more than half of the SI information is lost. By dividing the anode into 8 segments, the 8-anode detector can detect up to 8 SIs of the same m/z simultaneously if the SIs impact different segments of the anode. This greatly improves the detection efficiency, especially under massive cluster projectile impacts where abundant co-emission of SIs occurs.

Outputs from the detectors are routed into a constant fraction discriminator (CFD, Canberra, Meriden, CT). The CFD reforms the analog pulse outputs from the anode into logic square wave pulses and discards signals below a certain threshold, which are in most cases noises. Outputs from the CFD are fed into a time-to-digital converter (TDC) supplied by the Institut de Physique Nucleaire, Orsay, France. The TDC features one input for start signals and 8 inputs for stop signals, which can be used to accommodate signals from the 8-anode detector. Once a start signal is fed into the TDC, the timing mechanism starts recording arrival time of the stop signals within a preset data acquisition window. The arrival times are recorded in terms of channel numbers (250 or 400 picoseconds per channel). Digital outputs of channel numbers from the TDC are transferred to a computer and processed with the "Total Matrix of Events" (TME) software [85] to obtain a mass spectrum.

Event-by-Event Bombardment and Detection Mode

A distinct feature of the experiments carried out in this dissertation is the event-by-event mode of bombardment and detection. Under this scheme, a sequence of individual projectiles each strike "fresh" areas of the sample surface. There is no overlap in time or space between adjacent projectile impacts. SIs emitted from the specific projectile impact are recorded as an individual event in the computer. A mass spectrum is obtained by accumulating a certain number of such events ($\sim 10^6$). The SI yield for ions A (Y_A) under event-by-event mode operation is defined as:

$$Y_A(\%) = 100 \sum_{x_A} x_A I(x_A) / N = 100 \sum_{x_A} x_A P(x_A) \qquad \text{Eq. 3-10}$$

where x_A is the number of SIs of type A detected simultaneously per single

impact/emission event, x_A ranges from 0 to 8 in the experiments performed here due to the application of an 8-anode SI detector, and I_A is the number of events where ions A are detected. N is the total number of projectile impacts. P_A is the probability distribution of the number of ions A detected per impact/emission event. The above expression reduces to $Y_A(\%)=100P(1)$, when the most probable detection from an impact is at best a single SI, i.e., when $x_A=1$. This latter case is the one prevalent in the bombardment with atomic or small polyatomic projectiles. But under massive cluster projectile impacts, i.e., Au_{400}^{4+} and C_{60}^{+}, the emission of multiple identical ions is sufficiently frequent ($x_A>1$) that the SI yields must be computed based on the probability distribution $P(x_A)$.

Secondary ion multiplicity is defined as the number of SIs detected per impact/emission event [91,92]. When Au_{400}^{4+} is used to impact organic targets, the multiplicity distribution shows that on average there are 8-10 SIs detected per event [51]. Such abundant co-emission provides a good opportunity to investigate the relationship between coincidentally emitted SIs. Event-by-event bombardment/detection mode provides the capability of detecting co-emission from single events, since all events are stored individually. The coincidentally emitted SIs must originate from the same emission volume perturbed by a single projectile. Molecular dynamic (MD) simulations of cluster projectile impacts show that the projectile perturbs a region as small as ~ 10 nm in diameter and a few nm in depth. SIs emit from a volume with similar dimensions [59,93-95]. By looking at properties of the co-emitted SIs under event-by-event bombardment/detection mode, chemical information of the surface can be obtained from single impact region, i.e., ~ 10 nm in diameter.

One way to look at the relationship between co-emitted SIs is the correlation coefficient (Q) [96-98]. It is defined as follows:

$$Q_{AB} = \frac{\sum_{x_A}\sum_{x_B} x_A x_B P(x_A x_B)}{\sum_{x_A} x_A P(x_A)\sum_{x_B} x_B P(x_B)} = \frac{Y_{AB}}{Y_A Y_B}$$ Eq. 3-11

where $P(x_A x_B)$ is the probability distribution of the number of ions A and B detected simultaneously (emitted via single impact/emission event) and Y_{AB} is the corresponding coincidental yield of ions A and B. P_A, P_B and Y_A, Y_B follow the definition in SI yield (Eq. 3-10). If the emission of ions A and B is uncorrelated, i.e., A and B are emitted independently within the single impact/emission event, then the probability distribution $P(x_A x_B)$ is equal to $P(x_A)P(x_B)$, which results in Q_{AB}=1. When the emission of ions A and B is correlated; that is, the emission of ion A or B enhances the emission of the other one, Q_{AB}>1. If the emission of ions A or B suppresses the emission of the other, then the value of the correlation coefficient Q_{AB} will be lower than unity (anti-correlation). By looking at the values of the correlation coefficient (Q) from surface characteristic SIs, chemical information of the surface can be probed from single emission volume, i.e., ~ 10 nm dimension.

Sample Preparation

Layer-by-Layer Thin Films

The layer-by-layer film assembling technique was introduced in the early 1990s by Decher et al. [99,100]. It utilizes electrostatic interaction between charged polymers, proteins, and nanoparticles to form large-scale nanostructure on charged substrates [101-108]. In brief, a charged substrate (Si wafer, glass, or mica, usually with negative surface charge) is dipped into a dilute solution of a positively charged polyelectrolyte. A thin layer of the polycation is adsorbed onto the substrate spontaneously via electrostatic interaction. Since only the inner side of the adsorbed film interacts with the substrate, the outer side of the polyelectrolyte layer bears excessive positive charge. Thus, after adsorption, the surface charge property of the substrate is inversed. The substrate with the adsorbed polycation layer can then be
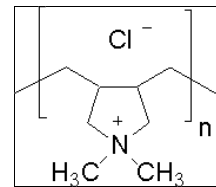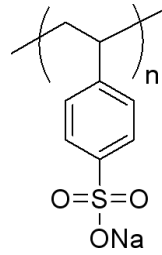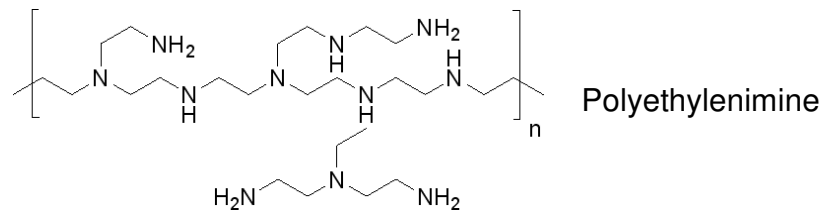
Figure 2-9 Structures of the polyelectrolytes.

dipped into a polyanion solution to adsorb another layer of the polyanion. The thickness of each adsorbed layer is at nanometer level. The adsorption cycle can be repeated for more than 100 times to obtain films with desired thickness and composition.

Two sets of thin layer films were used for the experiments mentioned in Chapter III. The first set of films used polyethylenimine (PEI, MW=1,800, 50% solution) and polystyrene sulfonate (PSS, MW=70,000) from Aldrich (Milwaukee, WI). Stock solutions of the polymers were at 3 mg/mL. Microscopic glass slides were cut into 1cm×1cm pieces and sonicated in an alkali cleaning solution (1:49:50, KOH:C_2H_5OH:H_2O) at 50 ℃ for 30 min. The cleaned glass slides were dipped immediately into the PEI solution for 20 min to obtain a 1-layer film. After dipping, the substrate was rinsed with copious amounts of water and dried under a N_2 stream. A 2-layer film was obtained by dipping a glass slide with a 1-layer film into the PSS solution for 20 min. One up to 10-layer films were prepared by dipping the glass slides alternatively into the PEI and PSS solutions.

The second set of films used polydiallyldimethylammonium chloride (PDDA, MW=200,000, 20% solution, Aldrich), in addition to the PEI and PSS (Figure 2-9). The concentrations of the polyelectrolytes were 5 mg/mL with 0.5 M NaCl. The added NaCl helps improve quality and thickness of the thin layer films. Si wafer pieces (Waferworld, West Palm Beach, FL) were cleaned with UV/ozone cleaner. The cleaned Si wafer pieces were first dipped into the PEI solution for 20 min, then rinsed with copious amounts of water, and dried under a gentle N_2 stream. This resulted in a 1-layer film. Si wafer with a 1-layer film was dipped alternatively into the PSS and PDDA stock solutions for 20 min to obtain films with the desired number of layers. The thicknesses of this set of thin layer films were tested with a Gaertner L2W26D ellipsometer (Gaertner Scientific, Skokie, Illinois) with a 632.8 nm laser beam and 70° incident angle. The cleaned Si wafer pieces were measured prior to film assembling to obtain substrate information. After assembling the desired

number of layers, the Si wafer was measured again to obtain the thickness data. The refractive indexes of all films were fixed at n=1.54 [101]. 4-5 spots on the sample surface were measured and an average thickness was obtained. The thicknesses of the films showed good reproducibility; a less than 10% variation was observed for 3 sets of films prepared. A thickness calibration curve was established to estimate the thicknesses of the thin layer films when the ellipsometer was not readily available.

The thin layer films analyzed in Chapter IV and V were assembled using PDDA, PSS and an inorganic nanoparticle: montmorillonite clay (STx-1, the Source Clays Repository, The Clay Minerals Society, Purdue University, West Lafayette, IN, $(Ca_{0.27}Na_{0.04}K_{0.01})[Al_{2.41}Fe(III)_{0.09}Mg_{0.71}Ti_{0.03}][Si_{8.00}]O_{20}(OH)_4)$. The negatively charged clay nanoparticle was purified according to the literature [105] and diluted to 0.5 mg/mL. Stock solutions for PDDA and PSS were 5 mg/mL with 0.5 M NaCl. Si wafer substrates (1cm×1cm) were first cleaned either with a UV/ozone cleaner or *Piranha Solution* (3:1, v:v, 98% H_2SO_4: 30% H_2O_2) at 70 ℃ for 15 min. The cleaned wafer was immediately dipped into the PDDA stock solution for 10 min, rinsed with water, and dried under a gentle N_2 stream; the resulting film was a 1-layer film. To obtain a 2-layer film, a 1-layer film was dipped into the PSS stock solution for 10 min. For films with more than 3 layers, the wafer with a 2-layer film was dipped alternatively into the PDDA and clay stock solutions, followed by rinsing and drying until the desired number of layers was assembled. 1 up to 12-layer films were assembled and tested. These films have been reported to be stable and retain their thicknesses in vacuum as in air [109]. The thicknesses of this set of films were measured with ellipsometry as mentioned above. X-ray photoelectron spectrometry (XPS) experiments were performed in the Materials Characterization Facility at Texas A&M University with a Kratos Axis Ultra Imaging XPS (Kratos Analytical, Chestnut Ridge, NY). The same set of 1 to 12-layer films used for SIMS analysis was tested with XPS for elemental composition information.

Vapor Deposition

Vapor deposition was used to prepare glycine (Fisher Scientific, Fair Lawn, NJ) thin film samples tested in Chapter VI. This method results in highly reproducible and uniform organic thin films on top of a stainless steel or brass sample cube.

Vapor deposition was carried out in a rectangular stainless steel vacuum chamber. The vacuum of the chamber was maintained by a Pfeiffer turbomolecular pump (240 L/s) backed by a 3 CFM rotary vane mechanical pump. The operational pressure of the chamber was $\sim 10^{-5}$ torr. The vapor deposition material was placed in an aluminum foil boat, which was heated by a 0-20 V, 0-45 amp DC power supply. After reaching working pressure ($\sim 10^{-5}$ torr), the Al boat was slowly heated to the sublimation temperature of the organic molecules. Heating was proceeded at low speed to avoid thermal degradation of the organic materials. Vapor deposition occurred when the cleaned and polished brass/stainless steel sample cube was coated with rings of glycine. When there were 4-6 rings on the surface, the heating current was cut off to avoid excessive coating, while the vacuum was maintained for an additional 5 to 10 min to allow the boat and sample cube to completely cool down.

Alkali Metal Ion Implantation

Alkali metal ion implantation experiments described in Chapter VI were performed in a house-built alkali metal ion implantation system (Figure 2-10). The alkali metal ion source (Cs^+ or Na^+, Heatwave Labs, Watsonville, CA, 1/4-inch diameter) was mounted on a stainless steel holder and placed 0.8-inch in front of the implantation target. A variable transformer was used to supply heating power to the ion source (ion emission temperature 800-1100 ℃). An extraction voltage was applied to the ion source in addition to the heating power through an isolation transformer. The extraction bias ranged from 50 V to 1 keV. A 1/4 inch-diameter collimator ($0.31 \ cm^2$ open area) was placed 0.2-inch in front of the target. A negative potential was applied to the collimator plate to suppress secondary electron emission
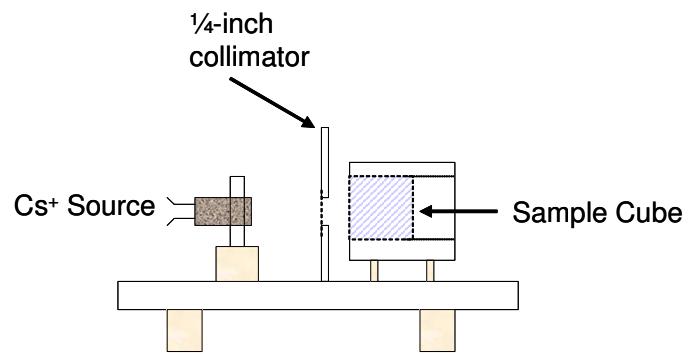
Figure 2-10 Schematic of the alkali metal ion implantation setup.

from the target during implantation. Brass/stainless sample cubes were held in a Teflon sample holder. The whole setup was assembled on a stainless steel platform and placed inside a vacuum chamber. The ultimate pressure inside the chamber was in the lower 10^{-6} torr range.

During operation, the Cs^+ (or Na^+) source was slowly heated to its emitting temperature. It was stabilized at this temperature for 20 min. Then the extraction bias and electron suppression bias were applied. Cs^+ (or Na^+) started emitting and impacting the target surface. The sample cube also acted as a Faraday cup to collect the implantation current, and a Keithley picoammeter was connected to the sample cube to measure the implantation current. Typically, the current was in the 0.05-0.2 μA range. The dose of the implanted alkali metal ions was calculated by integrating the implantation current with time, typical dose was in the 10^{15} ion/cm^2 range. The total implantation time ranged from less than 1 min to 40 min.

Vapor-deposited glycine samples were first analyzed with the 26 keV C_{60}^+ and/or the 136 keV Au_{400}^{4+} projectiles. They were then transferred into the alkali metal implantation chamber for alkali metal ion deposition. After implantation, the sample cubes were transferred back into the SIMS chamber for mass spectrometry analysis. A shadow with the shape of the collimator was observed on the target surface under high dose implantation.

CHAPTER III

LAYER-BY-LAYER THIN FILMS ANALYZED WITH PDMS

AND SMALL CLUSTER PROJECTILES[*]

Self-assembled mono and multilayers are uniquely suited to test the depth from which SI signals are emitted [110]. This Chapter addresses this issue with an examination of the SI emission induced by $CsICs^+$, Au_3^+, and ^{252}Cf fission fragment projectile impacts on a suite of multilayer thin film surfaces. The latter were prepared via alternate adsorption of oppositely charged polyelectrolytes. It has been shown that the electrostatic adsorption allows one to assemble a large number of layers and that the architecture of the films can be controlled by the assembly sequence [100]. The test samples prepared here consisted of multilayer assemblies of polycations, PEI, PDDA, and polyanion, PSS. There are few reports on the application of SIMS to the characterization of multilayer films assembled via electrostatic interactions [60]. Most analytical work on a variety of assemblies, including metal oxide nanoparticles, clay platelets, and proteins, has been carried out with atomic force microscope, quartz crystal microbalance, Fourier-transform infrared, UV-VIS absorption spectrometry, and optical ellipsometry [105,111-113]. We examine below the performance of polyatomic projectiles and fission fragments in the analysis of multilayers via secondary ion emission.

Multilayer films made of PEI and PSS were characterized using two instruments. The first system is equipped with a CsI cluster primary ion source [26]. The other one has a Au-LMIS [23,85]. For the CsI cluster ion source, 19 keV $CsICs^+$ cluster projectiles were used. For the Au-LMIS, 21 keV Au_3^+ cluster projectiles were used.

In all the experiments, the primary ion flux was within the "super" static regime (~ 10^3 primary ions per second).

Typical mass spectra of 5- and 6-layer films from impacts of the two primary ions are shown in Figures 3-1 and 3-2. Similar patterns of the spectra were obtained from the two types of primary ion impacts. Three major SI peaks at m/z=26, 80, and 183 were observed. The peak at m/z=26 corresponds to the CN^- group in the PEI. The peak at m/z=80 is due to the SO_3^- group in PSS and the peak at m/z=183 is from the monomer of PSS. For 5 and 6-layer assemblies, the yield for the three secondary ions used to track the PEI/PSS layers (m/z=26, m/z=80, and m/z=183) were five to ten times larger with 19 keV $CsICs^+$ or 21 keV Au_3^+ projectiles than with 19 keV Cs^+ or 21 keV Au^+.

For the 5-layer film bombarded with $CsICs^+$ projectiles (Figure 3-1a), the largest peak in the spectrum (except for the peak due to H^-) occurs at m/z=26, which is mostly due to the CN^- group in the PEI. In a 5-layer film, PEI is the outermost layer. In even-layered films such as a 6-layer assembly (Figure 3-1b), PSS is the outermost layer. Here, the most abundant secondary ion outside of hydrogen is m/z=80, which corresponds mostly to the SO_3^- group of PSS. Both spectra show that the outermost layer does not preclude the emission of ions from the polymer molecules underneath. For example, the mass spectrum from a 5-layer film, where PEI is the top layer, also shows fragment ions from the underlying PSS molecules.

For 5- and 6-layer films bombarded with Au_3^+ projectiles, the most prominent peak belongs to m/z=80 regardless of the type of polymer in the top layer (Figure 3-2a and 2b).

In Figure 3-3, we present the ratios of the peak areas corresponding to m/z=80 and 26 for different layers. Two trends can be observed: the oscillation in the ratio and the gradual increase of the ratio as the number of layers increase. These trends occur in spectra obtained from both $CsICs^+$ and Au_3^+ primary ion impacts.
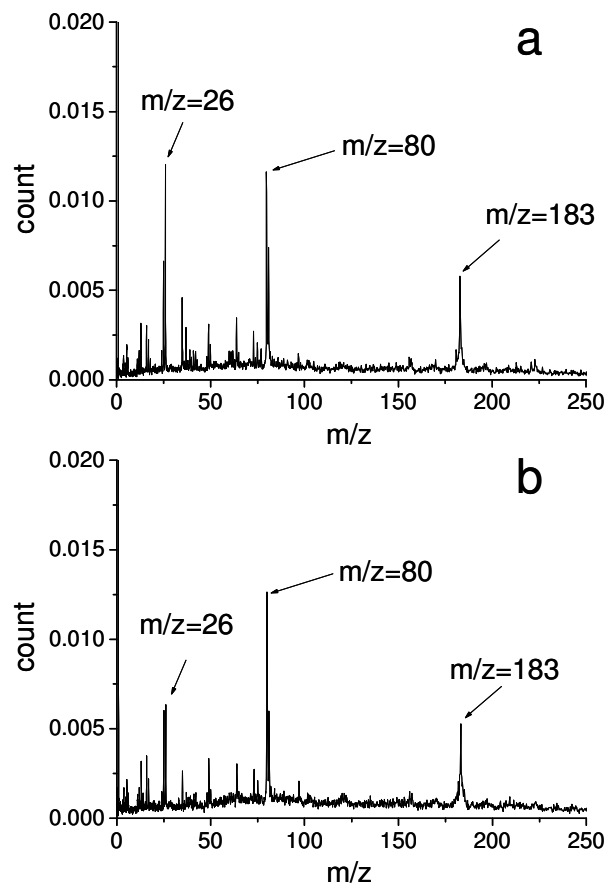
Figure 3-1 Negative ion mass spectra of (a) 5-layer (PEI/PSS)$_2$PEI film and (b) 6-layer (PEI/PSS)$_3$ film with 19 keV CsICs$^+$ projectile impacts. Counts are normalized to the total number events (~ 5×10^5 events).
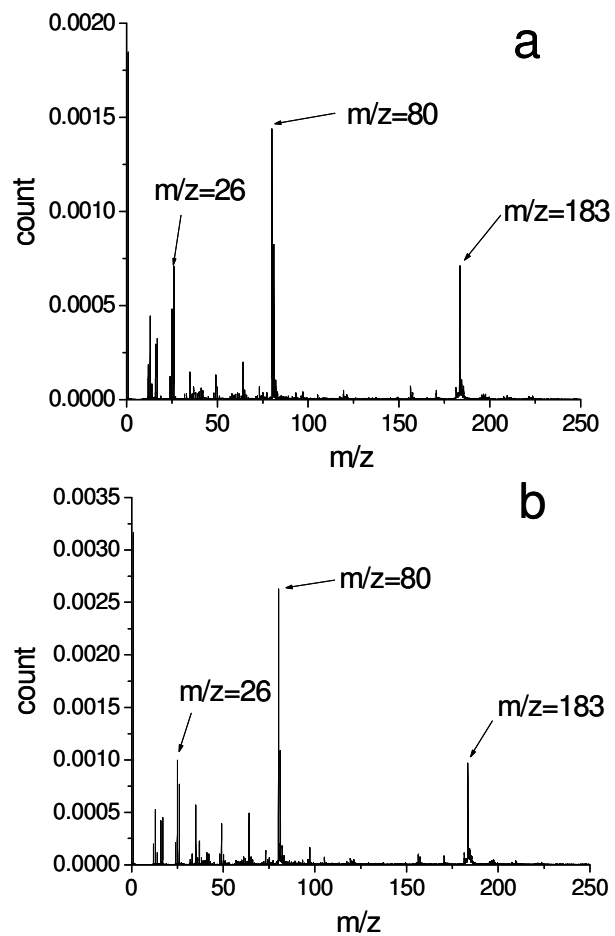
Figure 3-2 Negative ion mass spectra of (a) 5-layer (PEI/PSS)$_2$PEI film and (b) 6-layer (PEI/PSS)$_3$ film with 21 keV Au$_3^+$ projectile impacts. Counts are normalized to the total number of events (~ 1×10^6 events).
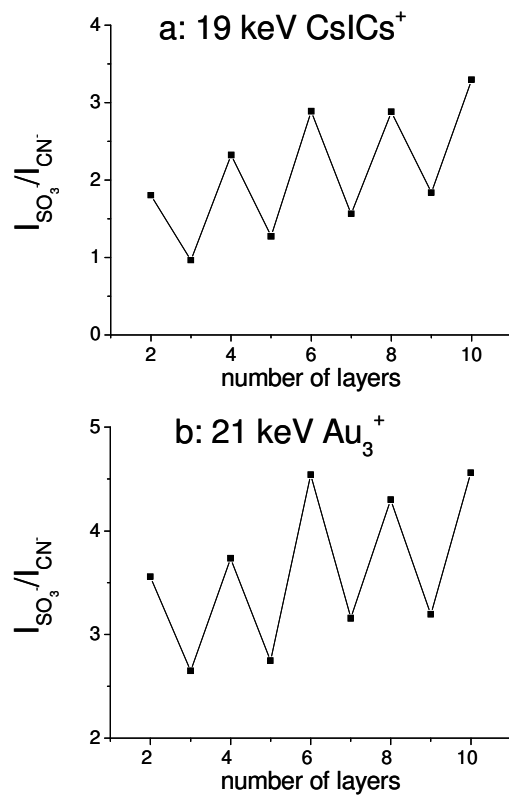
Figure 3-3 Ratio of peak intensity of m/z=80 and 26. (a) obtained from CsICs[+] primary ion spectra. (b) obtained from Au_3^+ cluster ion spectra.

The oscillation of the ratio with the number of layers is due to the difference of the relative position of the two film components (PEI and PSS). When PSS is in the outermost layer, the emission of SO_3^- is favored. Moreover, the SO_3^- group in PSS can be considered as a preformed ion, thus, its emission as anion is facilitated on physico-chemical grounds. When PEI is the outermost layer, the CN^- signal is, as expected, higher than when PEI is below PSS. However, it must be noted that PEI, regardless whether it is the topmost layer or not, always contains the $C-NH_2^+$ group. Clearly, it will be more difficult to obtain a negative ion from this positively charged group. Thus, the oscillation in the ratio of m/z=80 versus 26 reflects the relative position of PSS and PEI. The higher ratio for the even-numbered layers versus the adjacent odd-numbered layers relates to the physico-chemical characteristics of the PSS and PEI layers.

The increasing "baseline" for the successive ratio of the oscillations is due to an increase in the yield of SO_3^- with a growing number of the PSS layers. As mentioned earlier, the emission of SO_3^- is favored since it pre-exists as an anion in the PSS layers. The yields of CN^- vary little as the number of PEI layers increase. This again can be understood based on the physico-chemical environment in PEI. The constant yield in CN^- suggests that this species originates from the topmost PEI layer with little output added from the deeper PEI layers.

Another set of thin layer films made of PEI, PSS, and PDDA were prepared and analyzed with PDMS to test the depth of SI emission under fission fragment impacts. PEI was assembled at the first layer of the films with alternating PSS and PDDA layers on top of it. Ellipsometry was used to measure the thicknesses of the films (Figure 3-4). The thickness of each adsorbed layer is at nanometer (nm) level; the total thickness of a 13-layer film is more than 30 nm.

The most prominent peak besides H^- for a 1-layer PEI film is m/z=26 (Figure 3-5), while for the PEI/(PSS/PDDA)$_5$ 11-layer film, peaks at m/z=80 and 183 also show high intensities (Figure 3-6). SIs from the PSS layers show high intensities,
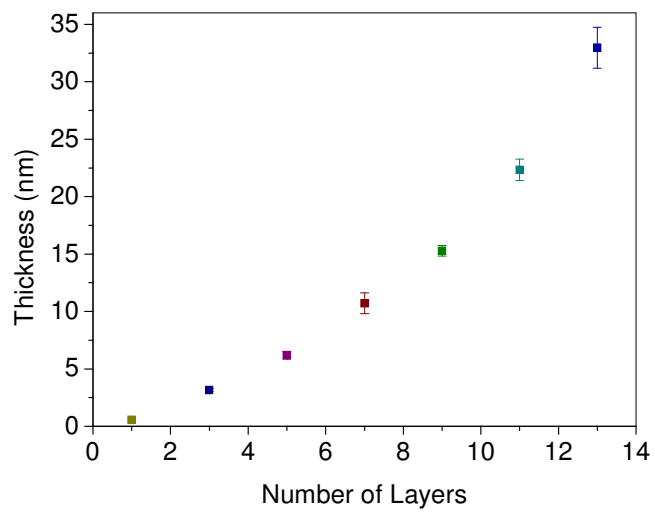
Figure 3-4 Thickness of the PEI/(PSS/PDDA)$_n$ (n=0-6) thin layer films measured by ellipsometry.
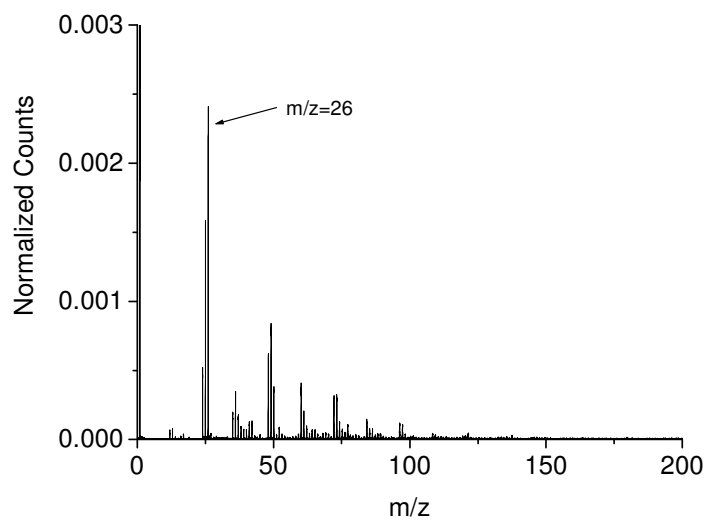
Figure 3-5 PDMS negative ion mass spectrum of 1-layer PEI film. Counts are normalized to the total number of events (~ 5×10^5 events).
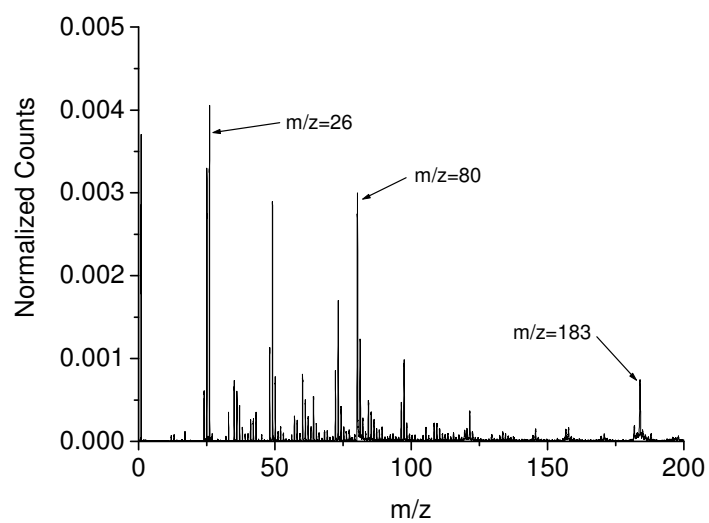
Figure 3-6 PDMS negative ion mass spectrum of 11-layer PEI(PDDA/PSS)$_5$
film. Counts are normalized to the total number of events ($\sim 5 \times 10^5$ events).

even though they are covered by the PDDA layer. The energetic fission fragment projectiles can penetrate through the PDDA cover layer and cause SI emission from the underlying PSS layers.

The evolutions of the SI yields of m/z=25, 26, 80, and 183 are shown in Figure 3-7. The yields show a "saturation" effect. The yields increase initially, due to the assembling of more layers into the films. When the films reach a certain thickness (9-layer film and beyond), the yields level off and tend to be stable. This suggests a limited depth of SI emission under fission fragment bombardments. After the 9-layer film, only layers located within the SI emission depth contribute to the SI signals detected. The total thickness of a 9-layer film is ~ 15 nm. The depth of SI emission with fission fragment impacts should be less than the thickness of a 9-layer film and remain in the ~ 10 nm range.
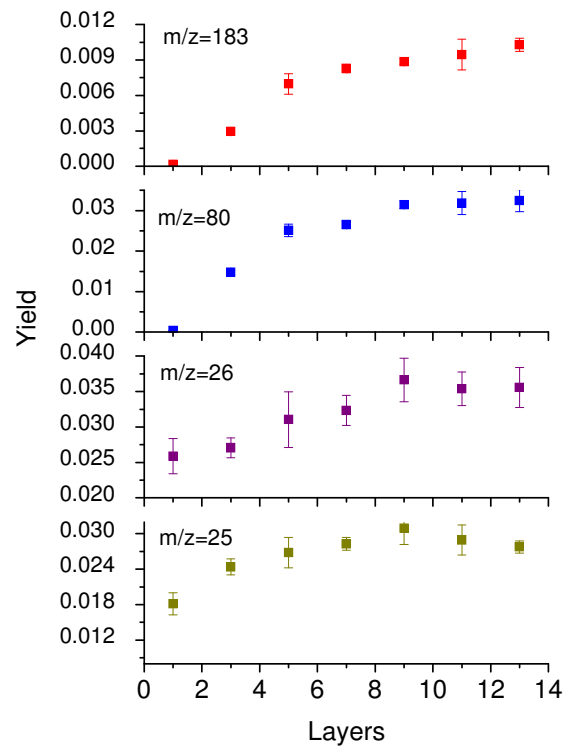
Figure 3-7 Evolution of SI yields with increment of layers.

CHAPTER IV

NANOVOLUME ANALYSIS WITH MASSIVE PROJECTILES[*]

As mentioned in the introduction, the SI yields can be increased by one to two orders of magnitude when a surface is bombarded by polyatomic instead of atomic projectiles [2,14,20,22,23,26,30,48,50,51,92,114-118]. Current efforts with SIMS instruments aim to obtain chemical information from dimensions in the submicron range. We present here an alternative which sidesteps the issue of focusing a beam, yet allows extracting chemical information from nanodomains. We used massive Au_{400}^{4+} projectiles under event-by-event bombardment/detection mode to analyze a set of specially designed thin layer films. At the level of an individual projectile impacts, the resulting SI emission will be from a nanovolume [24,95,96,98,119]. The correlations among co-emitted SIs arise when in the suite of volumes probed by successive projectiles. There are sites where the same chemical species are co-located.

The layer-by-layer films were assembled with PDDA, PSS, and clay nanoparticles on the Si wafers. A distinct feature of this set of thin layer films is the PSS indicator layer, which is placed at the second layer of the films with a varying number of PDDA/clay overlayers on top to investigate the depth of SI emission. The successive clay overlayers were analyzed to test planar homogeneity. One up to 12-layer films (Figure 4-1) were assembled and tested with 136 keV Au_{400}^{4+} projectiles. Ellipsometry was used to measure the thickness of the films (Figure 4-2).

Detection Sensitivity

Mass spectra of a monolayer of PSS with 136 keV Au_{400}^{4+} projectile
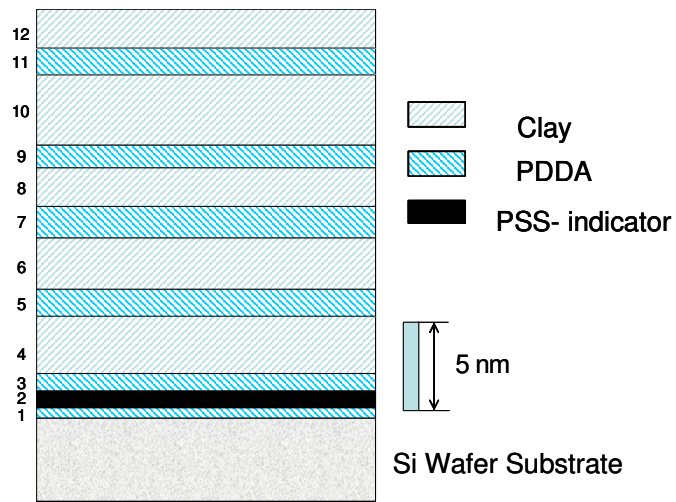
Figure 4-1 Illustration of a 12-layer film. Thickness drawn to scale.
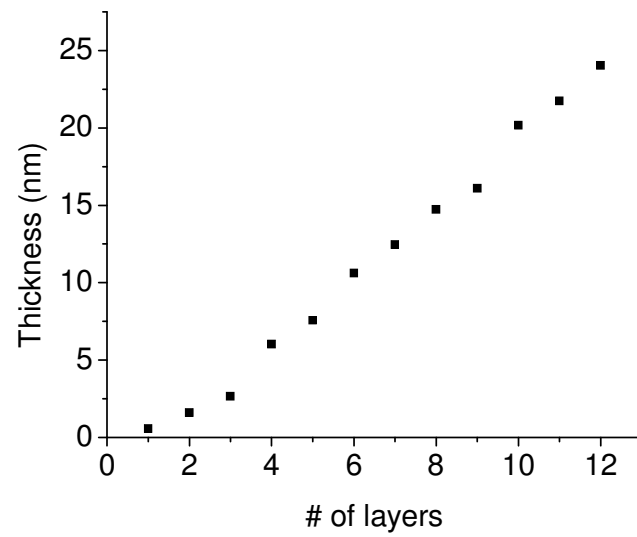
Figure 4-2 Thicknesses of the layer-by-layer films measured by ellipsometry.

bombardments are shown in Figure 4-3. In this case, the PSS was deposited on top of a monolayer of PDDA on a Si wafer substrate. The spectrum shows two major peaks at m/z=80 and 183. The lower mass signal is mainly due to SO_3^- from the PSS with a small contribution from the PDDA. The PSS produces a unique signal at m/z=183 corresponding to $CH_2CHC_6H_4SO_3^-$. A yield of 30% is measured for this species, i.e., 30 $CH_2CHC_6H_4SO_3^-$ ions are detected per 100 Au_{400}^{4+} projectile impacts. The spectrum shown in Figure 4-3a was obtained with a total of ~ 1×10^6 projectile impacts. Recalling that the area exposed to projectile impacts is ~ 1 mm^2, the bombardment occurred under "super-static" conditions, i.e., each Au_{400}^{4+} projectile impacts a fresh area of the target. The detection sensitivity is illustrated in Figure 4-3b. The mass spectrum shown here was obtained on the same target with the first ~ 1000 projectile impacts. Similar SI yields are obtained from the total spectrum and from the first ~ 1000 projectile impacts. We infer from these data that for the case at hand, i.e., for m/z=183, a few hundred projectiles are sufficient for a decision limit [120]. Anticipating on depth and lateral resolution data provided below, the cumulative volume sampled by a few hundred Au_{400}^{4+} projectiles contains ~ 1 attomol of the PSS monomer.

Depth and Volume Probed per Impact

The depth probing capability of the massive Au projectiles was determined by monitoring the peak at m/z=183 from PSS with a monolayer of the latter covered by varying numbers of PDDA and clay layers. As the number of layers on top of the PSS indicator layer increases, the SI signal intensity from the PSS layer decreases (Figure 4-4). For the 2-layer film, i.e., with PSS as the topmost layer, the yield of m/z=183 is nearly 30%. For the 3-layer film, the yield of these ions is slightly higher, although the PSS indicator layer is now covered by a 1 nm thick PDDA layer. This increased signal intensity might be due to the fact that the positively charged PDDA layer could enhance the ionization of the PSS layer, and thus facilitate the ionization and
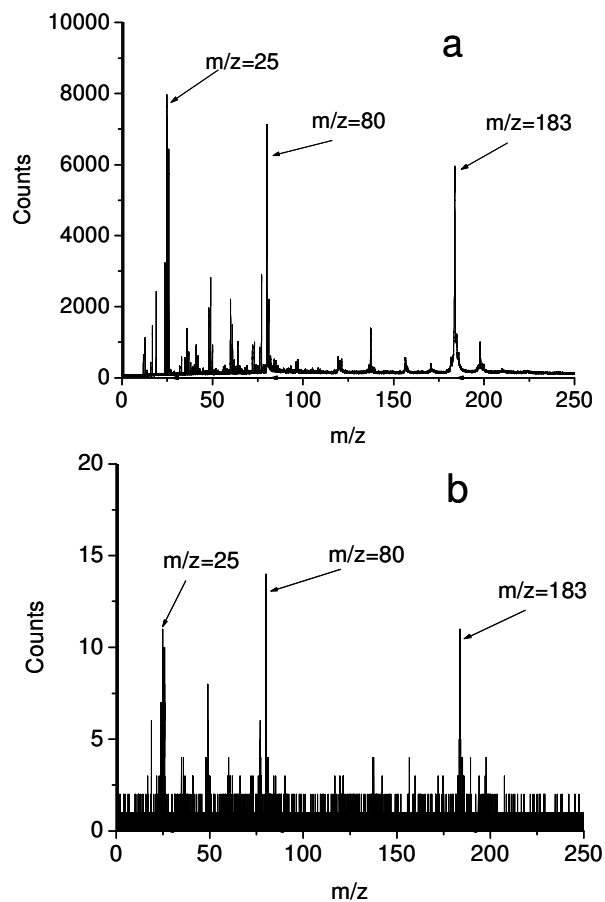
Figure 4-3 Negative ion mass spectra of 2-layer (PDDA/PSS) film from bombardment with 136 keV Au_{400}^{4+} projectiles. a) total spectrum obtained with ~ 1 million impacts, b) spectrum obtained with the first ~ 10^3 impacts.
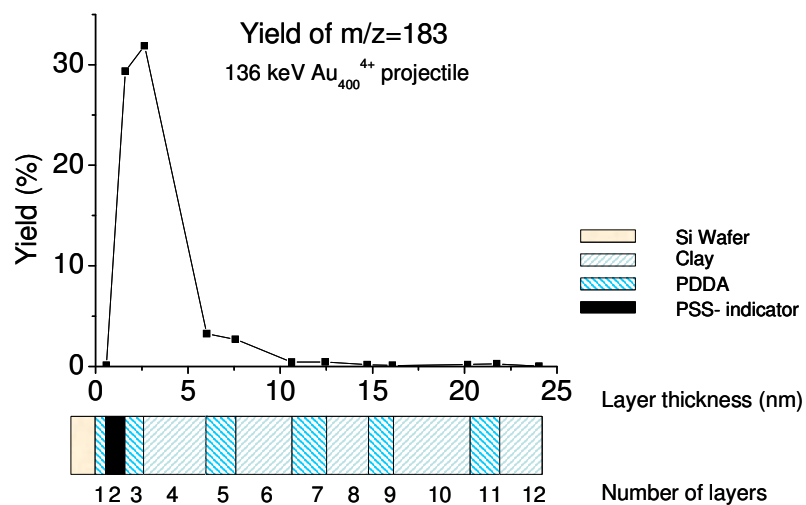
Figure 4-4 Evolution of the yield of m/z=183 ($CH_2CHC_6H_4SO_3^-$) with the number of layers. The x axis is drawn according to the thickness of each layer.

emission of ions from the underlying PSS layer.

In the case of a 4-layer film, that is when the PSS indicator layer is covered by a 4.4 nm thick PDDA/clay bilayer, the intensity of ions at m/z=183 decreases by 9-fold compared with the 2-layer film. However, for the 4- and 5-layer films, the ions at m/z=183 are still detectable, which means the massive Au_{400}^{4+} projectiles can still penetrate the PDDA/clay layers on top of the PSS layer and lead to the emission of SIs from the PSS layer. Thus, the 6.0 nm distance from the top of the 5th layer to the top of the PSS layer is still within the SI emission depth range. When more layers are added onto the PSS layer, i.e., for the 6-layer film and beyond, the intensity of ions at m/z=183 drops to background. This observation suggests that the SI emission depth for 136 keV Au_{400}^{4+} on soft polymer film targets is about 6-9 nm (the distance between the 2nd layer and the 5th layer is 6.0 nm and the distance between the 2nd layer and the 6th layer is 9.0 nm). This value is in agreement with MD simulation data [59,94,95].

The layer-by-layer resolution of SI signal is demonstrated by the evolution of the yields of ions m/z=77 (SiO_2OH^-) and 179 ((Al_2O_3)(SiO_2)OH^-) with the number of layers (Figure 4-5). A clear transition for m/z=77 is observed at the 3rd layer. The yield decreases prior to that layer and increases and oscillates beyond. This observation suggests that m/z=77 has two origins. For 1- to 3-layer films (without the clay layer), the emission of SiO_2OH^- from the Si wafer substrate is progressively blocked by the assembling of the PDDA and PSS films. The intensity of ions at m/z=77 for the 3-layer film is only 25% of that for the 1-layer film. Experiments on thick films of PDDA and PSS (>1 μm in thickness) showed no distinguishable peak at m/z=77. Thus, the decrease in the yield of ions at m/z=77 from 1-layer film to 3-layer film shows that the 2.6 nm thick PDDA/PSS film considerably decreases the emission of SIs from the Si wafer substrate. Nonetheless, the thickness of 2.6 nm is still within the SI emission depth of the Au_{400}^{4+} projectile. When the 4th layer, which is a clay layer, is adsorbed onto the film, the contribution of clay to the yield of ions

at m/z=77 is evident. Beyond the 4-layer film, the intensity of ions at m/z=77 increases with the addition of clay layers and tended to be stable beyond the 10-layer film.

The ions at m/z=179, i.e., $(Al_2O_3)(SiO_2)OH^-$, are mainly from the clay layers that contain 70% SiO_2 and 16% Al_2O_3. Indeed, for 1-, 2-, or 3-layer films, i.e., without clay layers in the assemblies, the signal at m/z=179 is practically near zero. For films with 4 layers or more, a trend similar to the ions at m/z=77 is observed. The similarity of the yields of ions m/z=77 and m/z=179 on 4-layer film and beyond confirms that for the films with more than 4 layers, the SiO_2OH^- ions are mostly contributed by the clay layers.

The intensities of both ions (m/z=77 and 179) are higher on clay-topped layers and lower on PDDA-topped layers (oscillation effect), and tend to be stable beyond the 10-layer film. For example, for the 9-layer film (PDDA-topped), the intensities of both ions are about 60% of those in the 8-layer film (clay-topped), while the intensities of these ions are similar for the 10- and 12-layer films. Thus, for the test case examined and the projectile characteristics used, the SI emission is in practice limited to the topmost 2-3 layers of the films. Most importantly, the characteristics of the topmost layer influence the type and intensity of the SIs emitted. We conclude that the SI emission depth is between 6-9 nm.

The shape of SI emission volume is likely to vary with the nature of the target. For carbon and graphite targets, a cylindrical structure seems to best approximate the emission volume. A molecular dynamic (MD) simulation of Au_{402} impacts at 100 eV/atom shows a virtually intact projectile at the bottom of a cylindrical crater [59]. Recent experiments with impact energies close to ours again show implantation of virtually intact projectiles, thus also suggest a cylindrical emission volume. Conversely, a MD simulation of C_{60} impacting a benzene layer at 250 eV/atom shows a semispherical crater with a diameter in excess of 10 nm [94]. For the samples studied here, we assumed a semispherical emission volume with a 6-9 nm
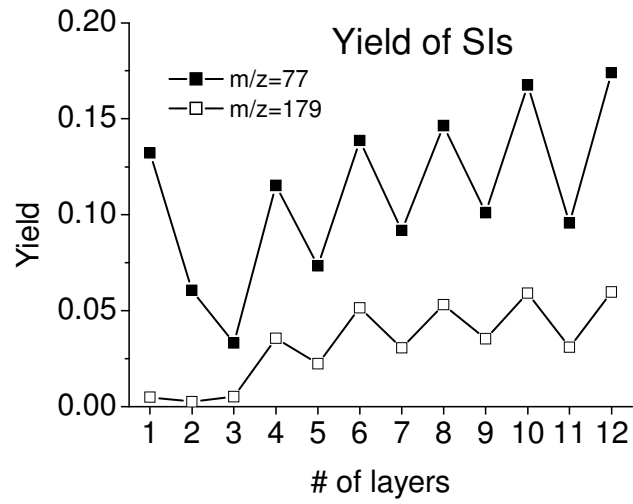
Figure 4-5 Yields of ions m/z=77 SiO_2OH^- and m/z=179 $(Al_2O_3)(SiO_2)OH^-$ obtained with 136 keV Au_{400}^{4+} bombardments and their relationship with the number of layers.

radius, which might be an overestimation.

Comparison of Small Au Cluster Projectiles with Massive Au Projectiles

The ability to extract information from single impacts is a distinct feature of the massive Au_{400}^{4+} projectiles. For comparison, we show in Figure 4-6 the results of the massive and small Au clusters on the same set of layers. Clearly, the small Au cluster projectiles are less efficient in SI yields, even though the kinetic energy carried by each Au atom is much higher. Starting with the 4-layer film, ions at m/z=183 are barely detectable with small Au cluster projectiles. Thus, the SI emission depth is more shallow for the smaller Au cluster projectiles tested here than for the massive Au projectiles.

Test of Nanovolume Homogeneity

As an example, let's look at the 4-layer film. The coincidental emission of SIs from the PSS indicator layer and the clay layer would indicate the emission depth is larger than the distance between the PSS layer and the clay layer. If there is no co-emission of PSS-related ions with clay-related ions, one could conclude that either the SI emission depth is less than the distance between the PSS layer and the clay layer, or these two film components are segregated spatially beyond the probing volume of the projectile. Thus, by monitoring coincidentally emitted SIs, the relationship of film components and homogeneity of the film can be investigated.

The physical relevance of co-emitted SIs is evaluated with the correlation coefficient, Q, which is defined as follows:

$$Q_{AB} = \frac{\sum\limits_{x_A}\sum\limits_{x_B} x_A x_B P(x_A x_B)}{\sum\limits_{x_A} x_A P(x_A) \sum\limits_{x_B} x_B P(x_B)} = \frac{Y_{AB}}{Y_A Y_B}$$

For example, let's consider the correlation coefficient for ions m/z=25 and 26 in the case of the 2-layer film. Ions with an m/z of 25 correspond to C_2H^-. They originate either from the polymer skeleton or from randomly adsorbed organic
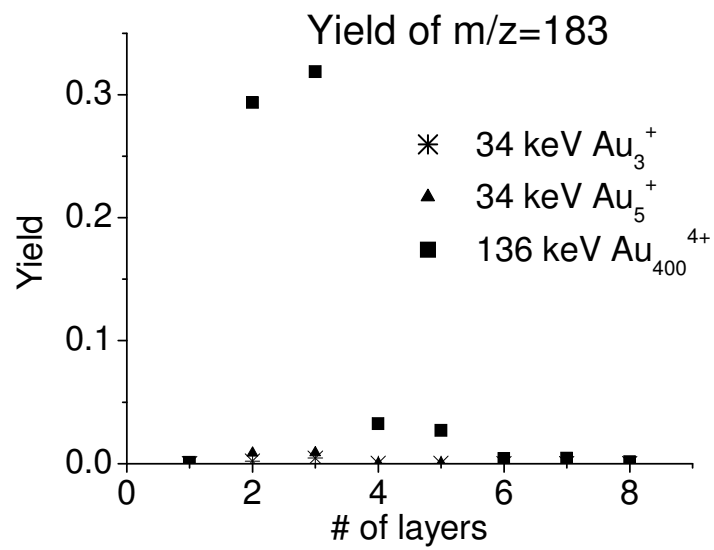
Figure 4-6 Yields of ions m/z=183 ($CH_2CHC_6H_4SO_3^-$) for 1- to 12-layer films with 34 keV Au_3^+, Au_5^+ and 136 keV Au_{400}^{4+} projectiles.

contaminants. Ions at m/z=26 are mainly due to CN^- from either the PDDA or contaminants. It may be assumed that the polymers together with the contaminants cover the surface in a uniform manner, i.e., the molecules from which these two ions originate are evenly distributed on the films. Accordingly, the co-emission of these two ions should be uncorrelated, i.e., the Q value should be unity. The experimental value obtained from the coincidental spectrum is 1.1, which is in agreement with the assumption.

The correlation coefficients for ions m/z=80 and 183 in the case of 2- to 5-layer films are presented in Table 4-1. For 2 and 3-layer films, the Q values are close to unity, which means, the emission of SO_3^- and $CH_2CHC_6H_4SO_3^-$ is not correlated. Furthermore, this result suggests that PSS is formed as a uniform layer on top of the Si wafer. Indeed, if the PSS did not form a uniform layer on the surface, the random impacts of Au projectiles over a probed area of ~ 1 mm^2 would result in two types of emissions, either with or without PSS-related ions. However, if the availability of PSS-related ions is equal at different locations of the surface, the emission of PSS-related ions follows a statistical distribution and the correlation coefficient will be unity. For 4- and 5-layer films, the correlation coefficients are higher than unity, which can be explained by the presence of the clay layer on top of the PSS layer.

High correlation coefficient values ($Q>1$) are also observed for clay-related ions on 4-layer film and beyond (Table 4-2), while low correlation coefficients ($Q<1$) are observed between PSS-related ions and clay-related ions for the 4-layer film (Table 4-3). These observations reveal a lack of homogeneity in the clay layers within the film. Such observations are consistent with the dimension and properties of clay nanoplatelets. Inspections of the clay nanoplatelets with TEM and XRD have shown that the clay nanoplatelets are about 50-100 nm in diameter and about 1.5 nm in thickness. When these nanoplatelets are assembled into layer-by-layer thin films, they are not as uniform as the PSS layer [105,121]. Instead, the clay platelets tend to aggregate and stack, thus, there are regions with multiple layers of clay platelets in

Table 4-1 Correlation coefficients (Q) of ions m/z=80 (SO_3^-) and 183 ($CH_2CHC_6H_4SO_3^-$) for 2- to 5-layer films.

# of layers	2	3	4	5
Q	1.1	1.1	6.4	6.4

Table 4-2 Correlation coefficients (Q) of ions m/z=119 ($Al_2O_3OH^-$) and ((Al_2O_3)(SiO_2)OH^-) for 4- to 8-layer films.

# of layers	4	5	6	7	8
Q	1.62	2.06	1.50	1.81	1.77

Table 4-3 Correlation coefficients (Q) of ions m/z=80 (SO_3^-) and 179 (Al_2O_3)(SiO_2)OH^-), and m/z=183 ($CH_2CHC_6H_4SO_3^-$) and 179 (Al_2O_3)(SiO_2)OH^-) for 4-layer film.

ions (m/z)	80 and 179	183 and 179
Q	0.73	0.76

the clay layers, while at other sites only one sheet of clay is adsorbed. The real thickness of a "stack" or "island" region is higher than the average thickness of the film measured by ellipsometry, while the thickness of a "base" region, where less clay platelets are adsorbed, is lower than the average thickness. Consider now for the 4-layer film, if a projectile impacts the "island" region, then due to the higher thickness at that region, it would be more difficult for the projectile to cause SI emission from the underlying PSS layer. Under such circumstances, most of co-emitted SIs would be related to the clay in the topmost layer. However, if the "base" region is impacted by a projectile, SIs from the PSS layer would be more easily ejected and detected, because the clay cover layer is not as thick as that in the "island" region. In this case, one can expect co-emission of PSS-related SIs. This is also the only location where co-emission of PSS-related ions and clay-related ions can occur. Indeed, nearly all events contribute to the emission of clay-related ions, regardless whether an "island" or a "base" region is impacted, while only events from a "base" region impact contribute to the co-emission of PSS and clay-related ions. Thus, the co-emission of these two types of SIs will be anti-correlated. The observed Q values of ~ 0.7 to 0.8 support this assumption (Table 4-3). In the case of co-emission solely from the PSS layer, only impacts in the "base" region contribute to emission and co-emission of PSS-related ions. Thus, the emission of PSS-related ions have to be correlated and a high Q value (>6) is observed (Table 4-1). When clay is present within the top 2 layers, all impacts generate clay-related ions, and hence co-emission of clay-related ions. However, when hitting a clay "island," co-emission of clay-related ions occurs with increased frequency. Consequently, a correlation coefficient larger than unity is expected. The experimental values indeed range from 1.5 to 2 for 4- to 8-layer films (Table 4-2).

The examination of co-emitted SIs and the calculation of correlation coefficients amount to probing the sample surface with nanometric resolution. Even though the projectiles are not focused and they impact the surface randomly, the

nanometer-sized SI emission volume allows resolving spatially related co-emitted SIs. The correlation coefficient calculation shows that with the emission volume probed (12-18 nm in diameter), the PSS layer is quite uniform in thickness, while the clay layer is not as uniform with overlapping of adjacent clay platelets causing islands on the surface.

CHAPTER V

LAYER-BY-LAYER THIN FILMS ANALYZED WITH C_{60}^{+}

PROJECTILES: DEPTH AND NATURE OF SI EMISSION

The depth of SI emission was examined on layer-by-layer thin films consisting of PDDA, PSS, and clay nanoparticles with 26 keV C_{60}^{+} projectiles. The layered assemblies also allow assessing the accuracy with which the SI signals track the compositional variation. We report here on SI signals affected by recoiled atoms from the C_{60} projectile and on an unexpected reversal in the oscillation of the intensities of the C^{-} and CH^{-} emissions from successive nanolayers. These observations are compared below with data obtained on duplicate samples from 136 keV Au_{400}^{4+} projectile impacts. The SIs examined are of low m/z, i.e., signals that are abundant in the emission from organic, polymeric, and biological materials. The experiments described below were performed in the event-by-event bombardment/detection mode, where a sequence of individual projectiles each strike an unperturbed area of the target, i.e., a manner analogous to how molecular dynamic (MD) simulations are carried out.

Depth of SI Emission

As mentioned in Chapter II, PSS served as the indicator layer to test the depth of SI emission. Mass spectra from 2- and 4-layer assemblies with 26 keV C_{60}^{+} projectile bombardments are shown in Figure 5-1. The peak of interest for locating PSS is that of its monomer at m/z=183. Its signal decreases radically from the 2- to the 4-layer assembly. The yield data plotted in Figure 5-2 show that the PSS signal disappears for 6-layer film and beyond.

The distance between the top of the PSS indicator layer and the 5th PDDA layer is ~ 6 nm, while the distance between the PSS and the 6th clay layer is ~ 9 nm. Thus
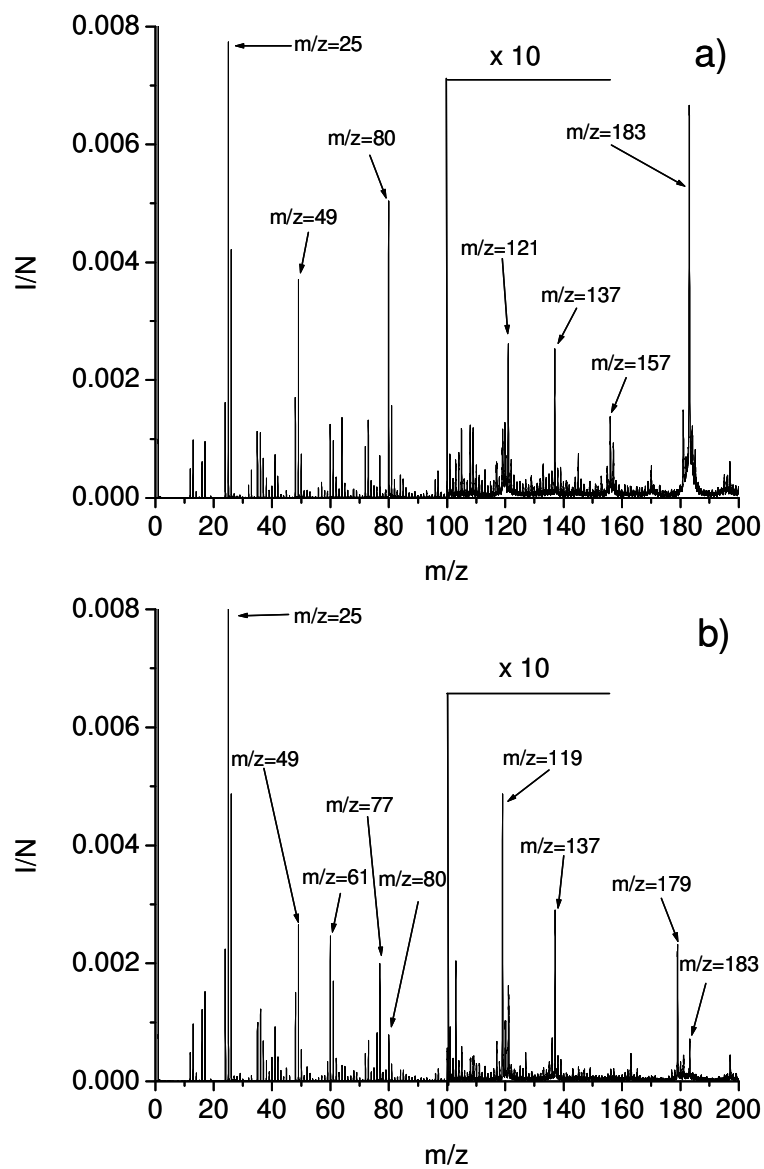
Figure 5-1 Negative ion mass spectra of: a) 2-layer PDDA/PSS film and b) 4-layer PDDA/PSS/PDDA/clay film analyzed with 26 keV C_{60}^{+} projectiles. Counts are normalized to the total number of events (~ 1×10^{6}).
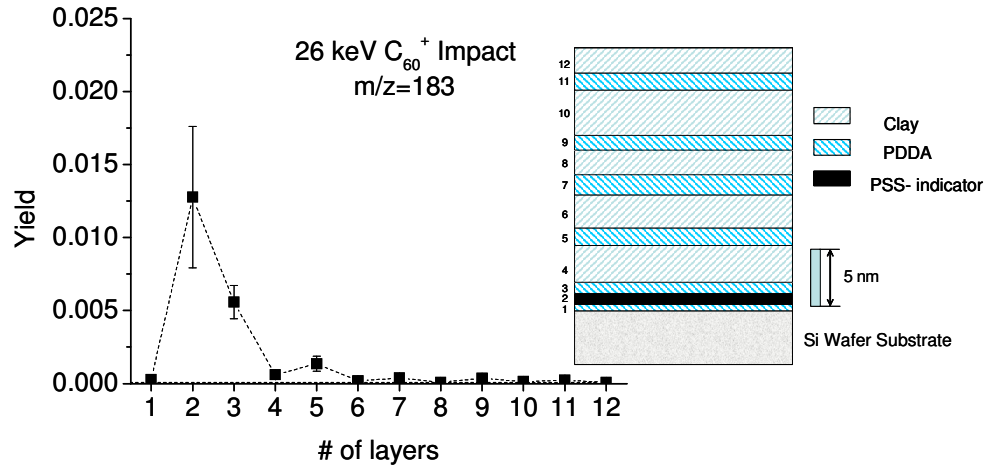
Figure 5-2 The SI yield of ions m/z=183 versus the number of layers. An illustration of the structure of a 12-layer film is shown on the right.

for the assemblies studied here, the SI emission depth is between 6-9 nm under 26 keV C_{60}^+ projectile impacts. A similar depth of emission has been reported when Au_{400}^{4+} projectiles of roughly comparable velocity impact these thin layer films [122]. A MD simulation of 5 keV C_{60} impacts on an organic surface shows a penetration depth of ~ 5 nm [57]. The crater formed after impact has a semispherical shape with ~ 15 nm in diameter and target constituents are emitted from a depth of ~ 10 nm.

The depth of emission can also be assessed by plotting the yields of SIs due to clay: SiO_2OH^- at m/z=77 and $(Al_2O_3)(SiO_2)OH^-$ at m/z=179. Figure 5-3 shows that the signal at m/z=179 is solely from the clay layer, indeed no signal above background is observed for 1- to 3-layer films when clay is absent. The yields of m/z=179 increase by ~ 30% between the 4- and 6-layer films, which indicates a contribution from the clay in the 4th layer to the SI signal. The signals tend to level off for 8-, 10-, and 12-layer films, suggesting that ions at m/z=179 are due mostly to the two topmost clay layers. The oscillation in the yields of m/z=179 illustrates the sensitivity of SIMS to surface composition. It should be noted that m/z=77 originates from the Si wafer for the low thickness films, but reflects only the presence of clay in the larger scale assemblies in a fashion similar to that observed for m/z=179.

Evaluation of Film Quality

Most of the SIs observed in the mass spectra show oscillation in a level range similar to that of m/z=179. An exception to this trend is observed for ions m/z=35, which are assigned to $^{35}Cl^-$. The chlorine ions are counter ions for the positively charged PDDA layers. The yields are higher for the odd numbered layers, i.e., when PDDA is the topmost layer. In contrast to the plateau observed for the yield of ions m/z=77 and 179 (Figure 5-3), the yield for ions m/z=35 keeps increasing for successive odd numbered layers (Figure 5-4 left axis). This trend is confirmed with XPS which shows an increase in the surface concentration of chlorine in successive PDDA layers (Figure 5-4 right axis). The information depth of XPS for organic
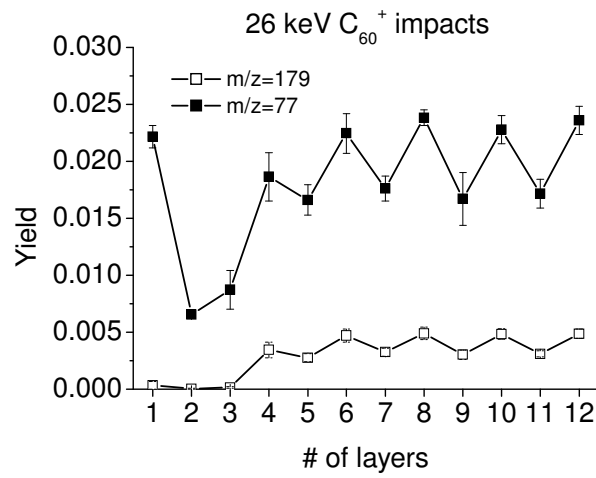
Figure 5-3 Oscillation of SI yields m/z=77 (SiO_2OH^-) and 179 ($Al_2O_3SiO_2OH^-$) with the number of layers.
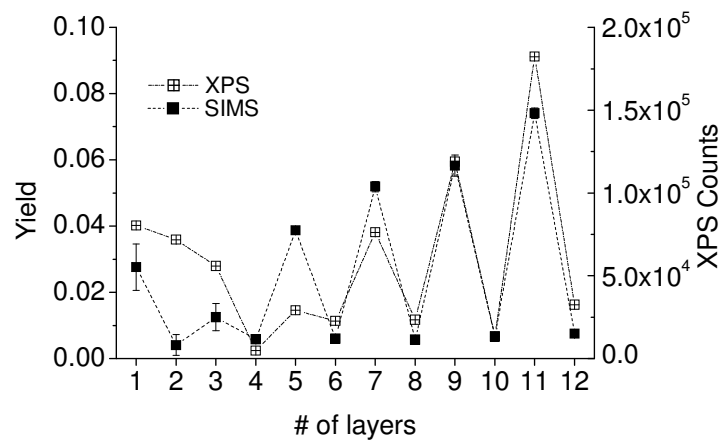
Figure 5-4 SI yields of $^{35}Cl^-$ (left axis) and XPS counts of Cl (right axis) versus the number of layers. SIMS results were obtained with 26 keV C_{60}^+ bombardment.

surfaces is in the range of 4-10 nm [123] and comparable to the depth of SI emission.

It has been shown that layer-by-layer films have "self-healing" properties, i.e., defects occurring at the initial stage of the assembling disappear with successive addition of overlayers [101]. The overall smoothness of the films increases with the number of layers assembled with a concomitant reduction in the total surface area. A steady state of SI yields is observed after the 8th layer for ions from clay (m/z=77 and 179). This indicates the packing densities of the film components remain constant with successive layer additions. Thus, a higher surface charge density is required to maintain a stable assembly with reduced surface area. The observation of increased Cl surface concentration from XPS and SIMS experiments suggests an increased surface charge density, and thus a better quality of the films as more layers are assembled. Again, SI signals at m/z=35 oscillate with the alternation of the topmost layers. This suggests most of the chlorine signals observed in SIMS originate from the topmost thin layer of the sample surface.

Influence of Recoiled Projectile Constituents on Yield Oscillations

The data presented so far and those published previously [122] show an oscillation of the SI yields reflecting the characteristics of the topmost layer (chemical composition, thickness).

A more complicated behavior of oscillations is observed for small carbon and hydrocarbon ions (Figure 5-5). First, the amplitude of oscillations decreases remarkably in the case of C_{60}^+ bombardments. Second, a reversed even/odd oscillation is observed for C^- and CH^- ions in the case of Au_{400}^{4+} projectile impacts (Figure 5-5a and b). The yields of these ions are higher when the clay layer is the topmost layer despite the absence of hydrocarbons in the clay layer. The "expected" order of oscillations is observed for C_2H^- and larger cluster ions (Figure 5-5c).

We can quantify the SI yield oscillations with the average of the ratio of higher yields to adjacent lower yields. The ratios, symbolized as K, are calculated for 5-layer
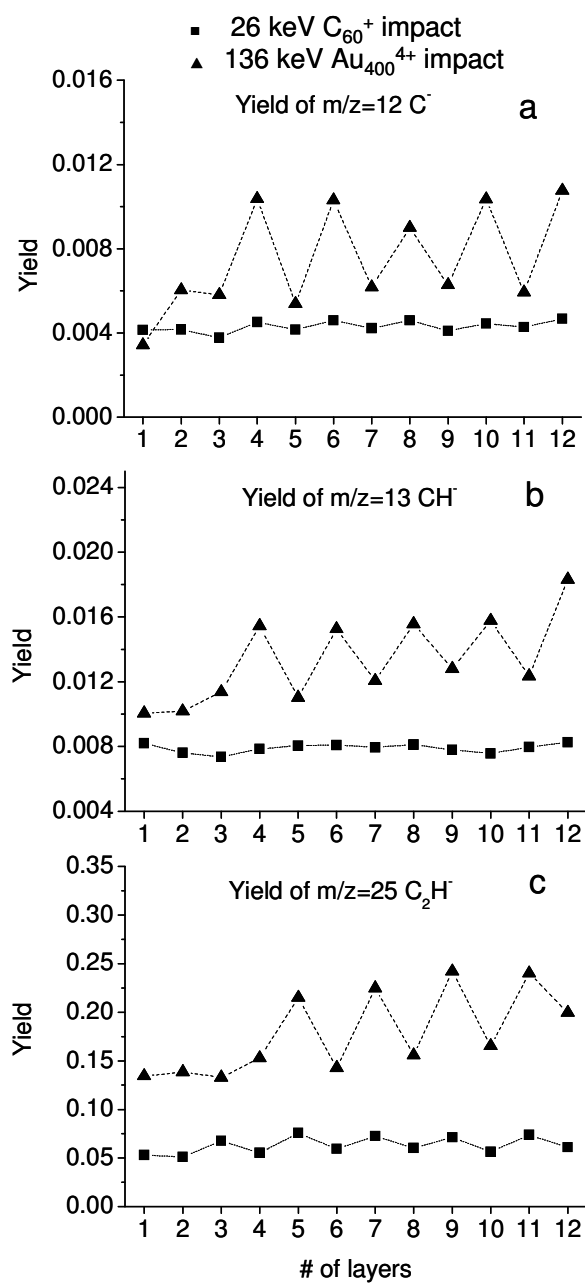
Figure 5-5 SI yields of m/z=12, 13 and 25 versus the number of layers obtained from bombardment with 26 keV C_{60}^{+} and 136 keV Au_{400}^{4+} projectiles. The C_{60} and Au_{400} TOF-SIMS instruments have similar transmission and detection efficiencies.

Table 5-1 Amplitude of oscillation (K) for selected SIs with 26 keV $C_{60}{}^+$ and 136 keV $Au_{400}{}^{4+}$ projectile impacts.

		26 keV $C_{60}{}^+$	136 keV $Au_{400}{}^{4+}$
m/z=12	C^-	1.09	1.71
m/z=13	CH^-	1.01	1.35
m/z=24	$C_2{}^-$	1.09	1.09
m/z=25	C_2H^-	1.24	1.40
m/z=26	CN^-	2.68	1.97
m/z=35	$^{35}Cl^-$	8.56	14.7
m/z=36	$C_3{}^-$	1.10	1.48
m/z=37	$^{37}Cl^-$ or C_3H^-	3.27	6.94
m/z=77	SiO_2OH^-	1.36	1.74
m/z=179	$Al_2O_3SiO_2OH^-$	1.59	1.91

films and beyond, where the films have long term stability. Table 5-1 shows the K values for different SIs generated by 26 keV C_{60}^+ (433 eV/atom) and 136 keV Au_{400}^{4+} (340 eV/atom) projectile impacts.

The K values are ~ 1 for small carbon clusters such as C^-, C_2^-, C_3^- and CH^- in the case of C_{60}^+ bombardments. The absence of "layer-specific" oscillation suggests that the carbon and small carbon cluster ions have a significant contribution from recoiled projectile constituents [124]. Evidence of the projectile constituents recoiling as ions with low kinetic energy has been observed previously in the mass spectrum of secondary ions from an organic surface bombarded with SiF_5^- [125]. A possible mechanism was discussed by Tombrello [126]. One should note that the present experiment and the SiF_5^- experiment were both performed in the "super-static" regime with extremely low doses of bombardment (~ 10^6 projectiles/mm^2) where the projectile strikes an unperturbed area of the target. Thus, the presence of recoiled CH^- ions (no oscillations) (Figure 5-5b, Table 5-1) indicates the extensive recombination processes in the expanding nanovolume of upward moving atoms, fragments of the analyte, and the shattered projectile. These results are consistent with recent MD simulations of C_{60} bombardment of hydrocarbon targets [57,58]. Concurrently, strong oscillations ($K >1$) observed for small carbon and hydrocarbon clusters in the case of Au_{400}^{4+} bombardment show that these clusters are secondary ions emitted from the topmost layers.

Another indication of the recoil emission and recombination is obtained from the comparison of the yields of Cl^- (m/z = 35 and 37) and C_3H^- (m/z = 37). As mentioned above, the chlorine is present in the PDDA layers (odd topmost layers) as the counter ion. However, the ratio of yields Y(m/z = 35)/Y(m/z = 37) is lower than the isotopic ratio of $^{35}Cl/^{37}Cl = 3.12$ for both projectiles (Figure 5-6). But, the ratios are always lower for C_{60} bombardments due to the contribution of C_3H^- recoils.

The most intriguing observation related to the yield oscillations is the reversed even/odd oscillations for C^- and CH^- ions with Au_{400}^{4+} projectile impacts (Figure
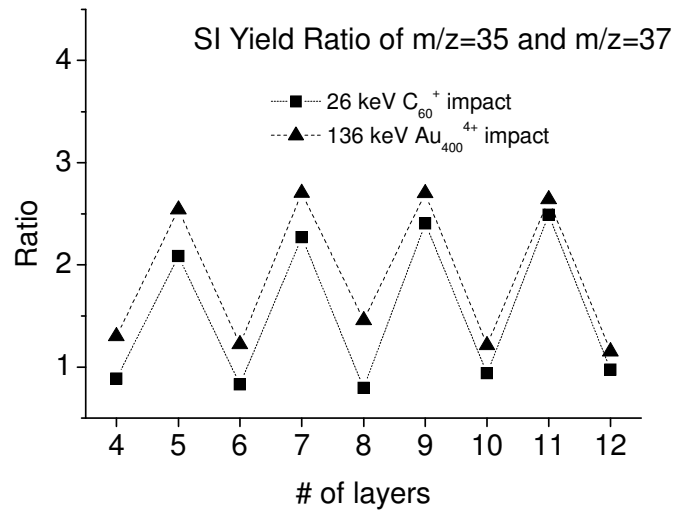
Figure 5-6 SI yield ratios of ions m/z=35 and 37 with 26 keV C_{60}^+ and 136 keV Au_{400}^{4+} impacts.

5-5a, b). This observation suggests a complex interaction process in the expansion volume. Such interaction results in a variety of emission/ionization mechanisms for different emitted species. Considering the depth of emission (~ 6-9 nm), it appears that the topmost clay layer does not screen the polymer layer below, hence the presence of polymer fragments in the collective outward motion and ion emission. Perhaps, the C and CH neutrals with low electron affinity (1.26 eV and 1.24 eV respectively) are ionized effectively by electron exchange processes, when colliding in the plume with metal atoms. In this scenario, the topmost clay layer provides the metal atoms that enhance the ionization probability of the C and CH. The mechanism proposed here is similar to that involved in the secondary ion yield enhancement stimulated by the metal deposition on the surface of analyte [127]. The effectiveness of the interaction is reduced when the polymer layer is on the top and the clay layer is on the bottom of the interaction volume. In this case the fast moving carbon atoms and small fragments exit the expansion volume before interacting with the metal atoms from the layer below. The larger carbon clusters and hydrocarbons have high electron affinities (>3 eV) resulting in higher ion yields regardless of the nature of the topmost layer.

CHAPTER VI

EFFECT OF ALKALI METAL ION IMPLANTATION

ON SI EMISSION

As mentioned in the introduction, in SIMS analysis, the deposition of Cs or the application of Cs^+ as primary ion beam reduces the surface work function and increases the negative SI yields. Most of the pertinent experiments reported so far were performed in the dynamic mode, where high intensity primary ion beams were used. A steady state is achieved when the Cs deposition rate and the sputtering rate reach equilibrium. However, it is difficult to measure the Cs^+ surface concentration at the equilibrium under dynamic SIMS bombardments. To date, there is no report on the effect of Cs^+ deposition in the super-static regime. Yet several issues are of interest: do the implanted alkali metals induce surface damage and result in decrease in SI yield, or do they facilitate the emission of SIs and compensate for such surface damage? What is the optimal implantation depth for the alkali metal ions to maximize the enhancement effect? Or is surface deposition (soft-landing) the preferred method to deliver alkali metals instead of implantation?

We present here some initial investigations of the effect of *ex situ* alkali metal implantation on SI emission. Organic targets were pre-implanted with Cs^+ of known kinetic energy and dose. This pre-implantation method allows controlling the Cs^+ surface concentration and the Cs^+ implantation energy, and thus the implantation depth.

We tested the effects of *ex situ* alkali metal implantation on SI yields on glycine surfaces. The vapor-deposited glycine targets were first analyzed with 26 keV C_{60}^+ and 136 keV Au_{400}^{4+} projectiles. They were then transferred into the alkali metal implantation chamber for implantation. After implantation, the targets were transferred back into the SIMS chamber for analysis. Na^+ was used to compare with

Cs^+ to investigate the performance of different alkali metal ions.

For a pristine glycine sample (Figure 6-1a), the major SIs observed include m/z=26 (CN^-) and 42 (CNO^-), which are the fragmentation/recombination ions of the glycine, m/z=74 (glycine molecular ion) and m/z=149 (glycine dimer ion). After a moderate amount of Cs^+ (7.3×10^{14} ions/cm^2 at 1 keV) is implanted onto the surface (Figure 6-1b), the SI signals at m/z=74 and 149 decrease, while the signals at m/z=26 and 42 remain nearly constant. When the Cs^+ dose increases to 8.2×10^{15} ions/cm^2, the SI signals of m/z=74 and 149 drop drastically (Figure 6-1c), especially in the case of the glycine dimer ions, the yield decreases by 75% (only 25% of the SI signal is observed compared with the pristine sample). The signal intensities of ions m/z=26 and 42 remain relatively constant. A similar decrease in the yields of glycine molecular and dimer ions is observed when using 136 keV Au_{400}^{4+} projectiles (Figure 6-2) with Cs^+ beam at relatively low energy and intensity (100 eV, 1.6×10^{15} ions/cm^2). After Cs^+ implantation, only 74% of the SI signal at m/z=74 is observed, while for the m/z=149, only 21% is left. In contrast, for the CN^- and CNO^-, the signal intensities increase. The same sample analyzed with C_{60}^+ projectile impacts show a different behavior, the SI yield of the glycine molecular ions remains nearly the same as before implantation, and the signal for the dimer ions decreases by less than 20% (with Au_{400}^{4+} impacts, that value is 80%). The fragmentation/recombination ions also remain nearly constant before and after implantation (Figure 6-3).

The yield change ratio (K) is used to compare the effect of Cs^+ implantation. K is defined as the ratio of the yield of a certain SI before and after Cs^+ implantation. If the K value is higher than 1, then the yield of the SI increases after implantation; if the K value is lower than 1, the yield of that SI decreases with the implantation of Cs^+. The K values of four SIs with C_{60}^+ and Au_{400}^{4+} projectile bombardments are shown in Figure 6-4.

$$K = \frac{Y_{After}}{Y_{Before}}$$

Figure 6-1 Negative ion mass spectra of vapor-deposited glycine analyzed with 26 keV C_{60}^+. a) pristine glycine, b) glycine after implanted with 2.3×10^{14} (7.3×10^{14} ions/cm^2) Cs^+ at 1 keV, and c) glycine after implanted with 2.6×10^{15} (8.2×10^{15} ions/cm^2) Cs^+ at 1 keV. Counts are normalized to the total number of events (~ 1×10^6 events).

Figure 6-2 Negative ion mass spectra of vapor-deposited glycine analyzed with 136 keV Au_{400}^{4+}. a) pristine glycine, and b) glycine after implanted with 5.0×10^{14} (1.6×10^{15} ions/cm^2) Cs^+ at 100 eV. Counts are normalized to the total number of events (~ 1×10^6 events).
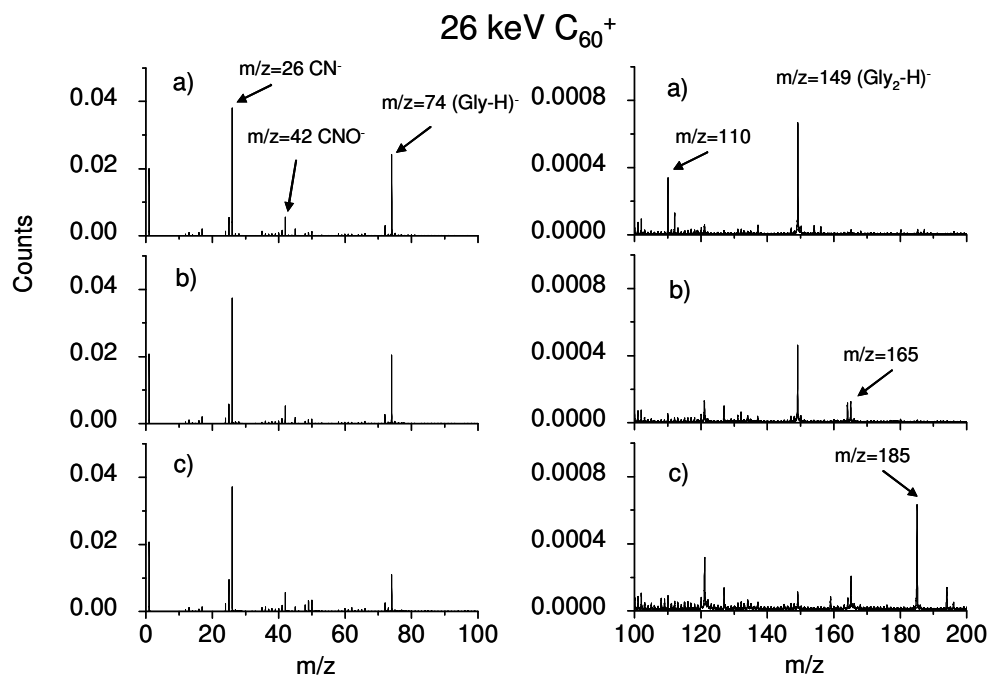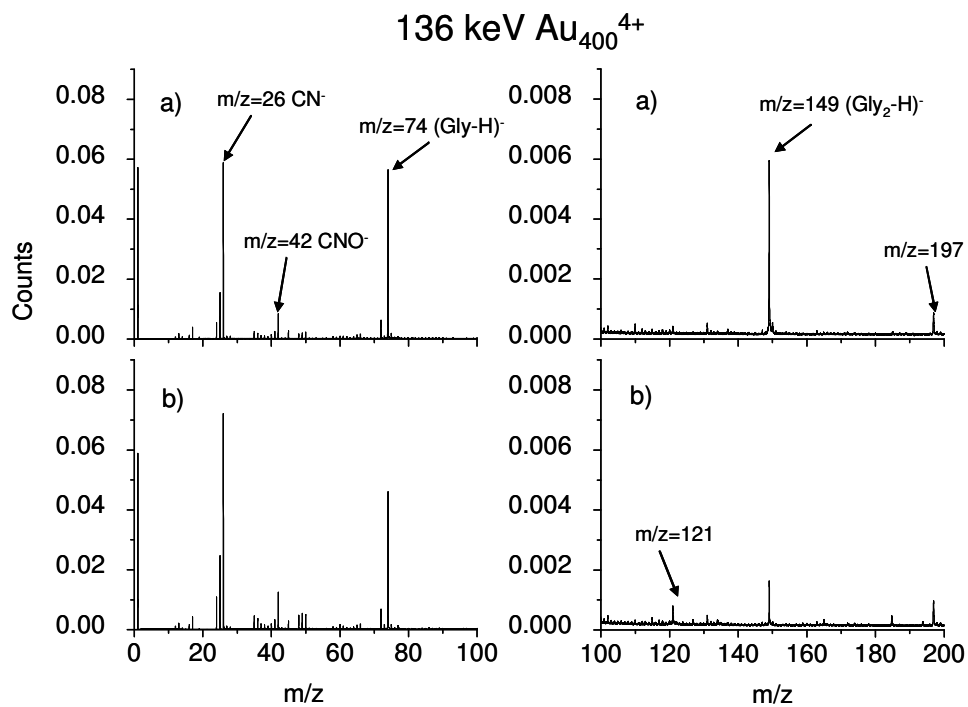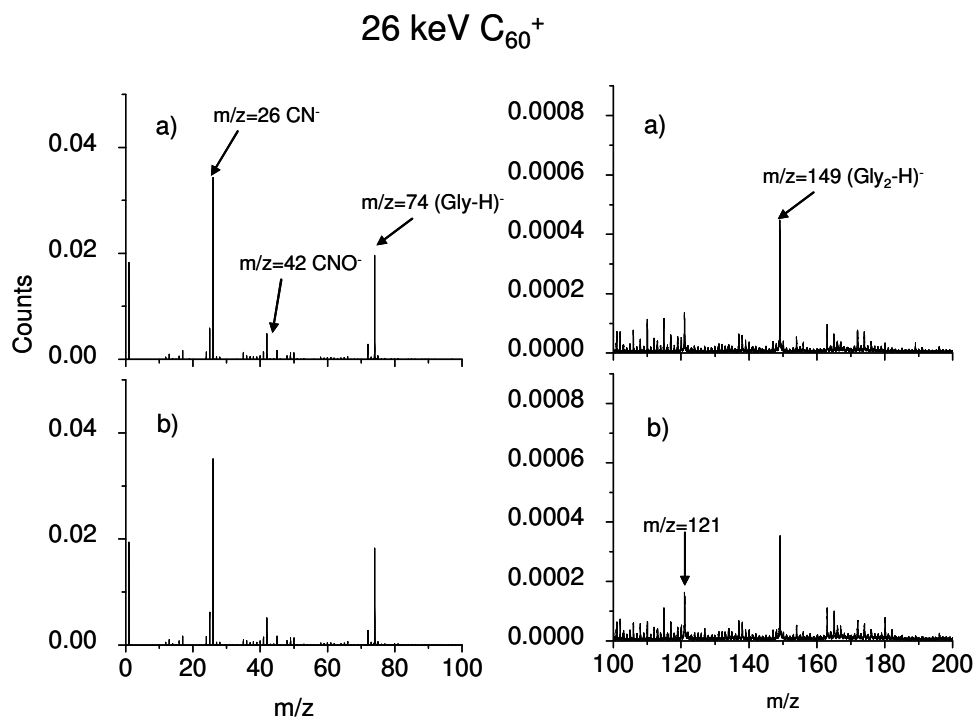
Figure 6-3 Negative ion mass spectra of vapor-deposited glycine analyzed with 26 keV C_{60}^+. a) pristine glycine, and b) glycine after implanted with 5.0×10^{14} $(1.6 \times 10^{15}$ ions/cm$^2)$ Cs$^+$ at 100 eV. Counts are normalized to the total number of events ($\sim 1 \times 10^6$ events).

In general, the K values for glycine molecular and dimer ions decrease after Cs^+ implantation, and the K values are lower with increased Cs^+ beam energy and dose. In contrast, for CN^- and CNO^-, which are mostly fragmentation/recombination ions from glycine, the K values are higher than unity and tend to increase with Cs^+ beam energy and dose.

When the Cs^+ (50 eV to 1 keV in kinetic energy) beam impacts a glycine surface, the Cs^+ interacts with the glycine molecules through collision and results in bond cleavage of the glycine molecules (typical bond energy is less than 10 eV). Thus, the surface undergoes significant collision-induced damage during implantation. SRIM (Stopping Range of Ions in Matter) [128] simulation shows that the penetration depths of Cs^+ are in the nanometer range on organic targets (Table 6-1). The targets used in the simulation closely represent the compositions and densities of organic samples like glycine studied here. The penetration depth of Cs^+ is at most ~ 7 nm with 1 keV impact energy. There is also ~ 1.5 nm in longitudinal straggling. Thus, after implantation, most of the Cs^+ ions are located within a narrow band (~ 3 nm) centered at the penetration depth, while glycine molecules are damaged along the Cs^+ trajectory.

Higher Cs^+ implantation energy results in deeper penetration depth; a higher dose causes more damage through the penetration pathway. Such damage results in fewer intact glycine molecules within the track of the Cs^+ beam. If the Cs^+ penetration depth is within the SI emission depth, the glycine molecular ion yield is expected to decrease with the increasing implantation energy and dose. In contrast, if the penetration depth is higher than the SI emission depth, the glycine molecular ion yield and the K value should be constant. Indeed, the K values of glycine molecular ions are similar under Au_{400}^{4+} bombardment when using both 100 eV and 200 eV Cs^+ beams with high intensity (~ 3.0×10^{15} Cs ions/cm^2). This means the 100 eV Cs^+ beam is sufficient to induce damage to the glycine molecules located within the glycine molecular ion emission volume. The emission of glycine molecular ions is
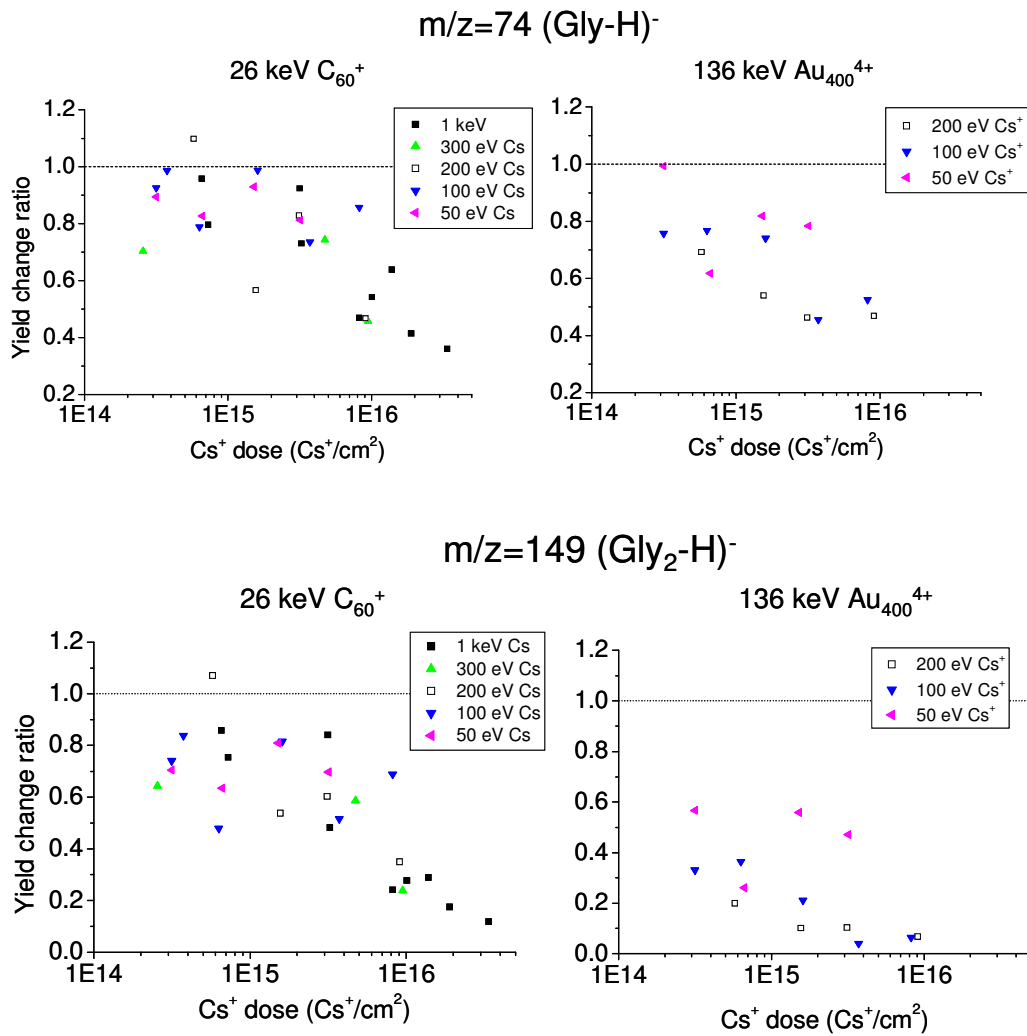
Figure 6-4 Yield change ratio (*K*) for selected SIs.

m/z=26 CN⁻

m/z=42 CNO⁻
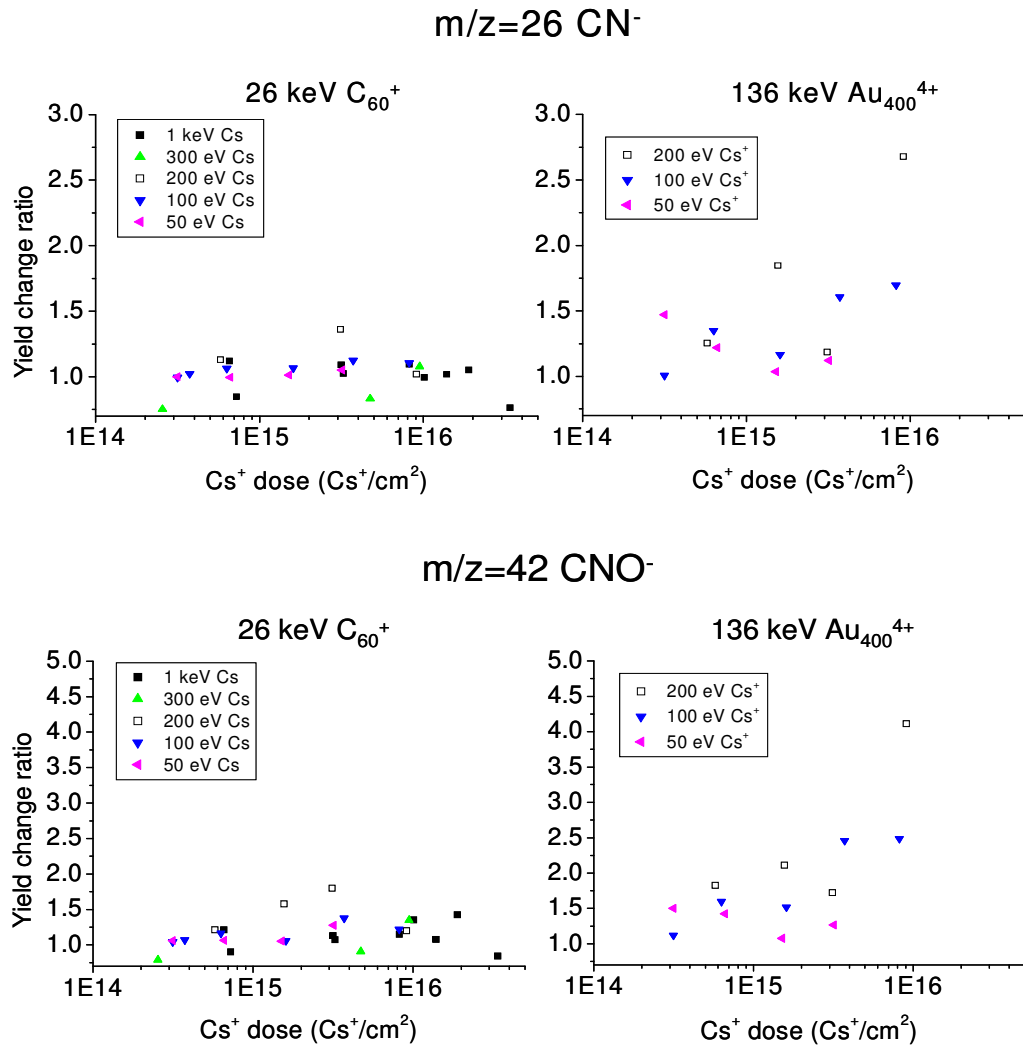

Figure 6-4 (continued)

Table 6-1 SRIM simulation of Cs^+ penetration depth in Mylar and Nylon, longitudinal straggling in brackets.

Cs^+ beam energy	Penetration depth (nm)	
	Mylar	Nylon
50 eV	1.7 (0.4)	2.1 (0.5)
100 eV	2.2 (0.5)	2.7 (0.6)
200 eV	2.9 (0.7)	3.5 (0.8)
300 eV	3.4 (0.8)	4.1 (1.0)
1 keV	5.6 (1.3)	6.7 (1.6)

thus mostly from the topmost ($\sim$ 2.5 nm) layer of the surface (Table 6-1). The emission of glycine dimer ions appears to originate from a similar depth because a similar trend of the K values is observed. The K values are lower for the dimer ions because the formation of dimer ions requires the co-existence of two intact glycine molecules within the emission volume. The K values for fragmentation/recombination ions (m/z=26, 42) increase after Cs^+ implantation with Au_{400}^{4+} bombardment. This is because the incoming Cs^+ beam destroys the glycine molecules and increases the availability of glycine fragments. The Cs^+ beam with higher kinetic energy results in higher K values. Higher K values are also observed when using a higher dose beam with the same implantation energy. This suggests that the CN^- and the CNO^- ions come from a volume deeper than that of the molecular ions. Thus, when using massive Au_{400}^{4+} projectile to probe a sample surface, the emission of large intact molecular ions comes form a shallower volume, or maybe rim of the crater. On the contrary, fragmentation/recombination ions come from a deeper volume of the crater.

When using the C_{60}^+ projectile instead of Au_{400}^{4+}, a different scenario is observed. For example, with a 100 eV Cs^+ beam and implanting 1.6×10^{15} ions/cm^2 Cs^+ , the K values for glycine molecular and dimer ions are 0.99 and 0.82 respectively with C_{60}^+ projectile impacts. In contrast, the K values are 0.74 and 0.21 respectively with Au_{400}^{4+} projectile impacts. Moreover, the K values for CN^- and CNO^- are 1.07 and 1.06 with C_{60}^+, while with Au_{400}^{4+} projectile impacts, they are 1.17 and 1.52 respectively. A gradual decrease in the K values for glycine molecular ion with increasing Cs^+ dose is observed when the kinetic energy of the Cs^+ beam increases to 1 keV. While when using lower energy Cs^+ beams, i.e., <100 eV, the K values are all in the $\sim$ 0.8 range regardless of the Cs^+ dose. Similar trend is also observed for the glycine dimer ions. This suggests that with the C_{60}^+ projectile bombardment, the emissions of the glycine molecular and dimer ions are from a volume comparable to the penetration depth of the 1 keV Cs^+ beam ($\sim$ 7 nm). The K values for

fragmentation/recombination ions (m/z=26 and 42) are close to unity regardless of the Cs^+ energy and dose with C_{60}^+ bombardments. This suggests the emissions of CN^- and CNO^- ions are mostly from the top of the surface (~ 2 nm). The implanted Cs^+ resides deeper than the emission depth of the CN^- and CNO^- ions, so that they are not involved in the ionization/emission process and no enhancement effect from the Cs^+ is observed. These data suggest that the SI emission with C_{60}^+ projectile impacts is different from that with Au_{400}^{4+} impacts.

A Na^+ ion beam was used to compare the performance of different alkali metal ions. Mass spectra of the glycine after implanting with 500 eV and 100 eV Na^+ are shown in Figures 6-5 and 6-6 under Au_{400}^{4+} and C_{60}^+ projectile bombardments respectively. The lower energy Na^+ beam (100 eV) considerably decreases the glycine molecular and dimer ion signals, while the higher energy beam (500 eV) sputters off all species on the surface. The mass spectra obtained resemble those of clean metal surfaces, which are dominated with small carbon cluster ions from contamination.

The *K* values of the SIs characteristic to the glycine are shown in Figure 6-7. It is observed that with the 500 eV Na^+ implantation beam, the glycine surface undergoes significant damage. When using C_{60}^+ projectiles to probe the implanted surface, the yields of all SIs characteristic to the glycine drop drastically, and the *K* values are in the range of 0.1-0.2. The same sample analyzed with Au_{400}^{4+} projectiles shows a similar decrease in the glycine and dimer ion yields, but a small increase is observed for the fragment ions (m/z=26 and 42). Such discrepancy in the *K* values again suggests different mechanisms of the SI emission with C_{60}^+ and Au_{400}^{4+} projectile impacts.

For the lower energy Na^+ implantation beam (100 eV), *K* values less than unity are observed for the glycine molecular and dimer ions with both projectiles impacts. The *K* values are lower with the Na^+ beam than with the Cs^+ beam at equal implantation energy (Figure 6-7). This suggests the Na^+ beam induces more surface
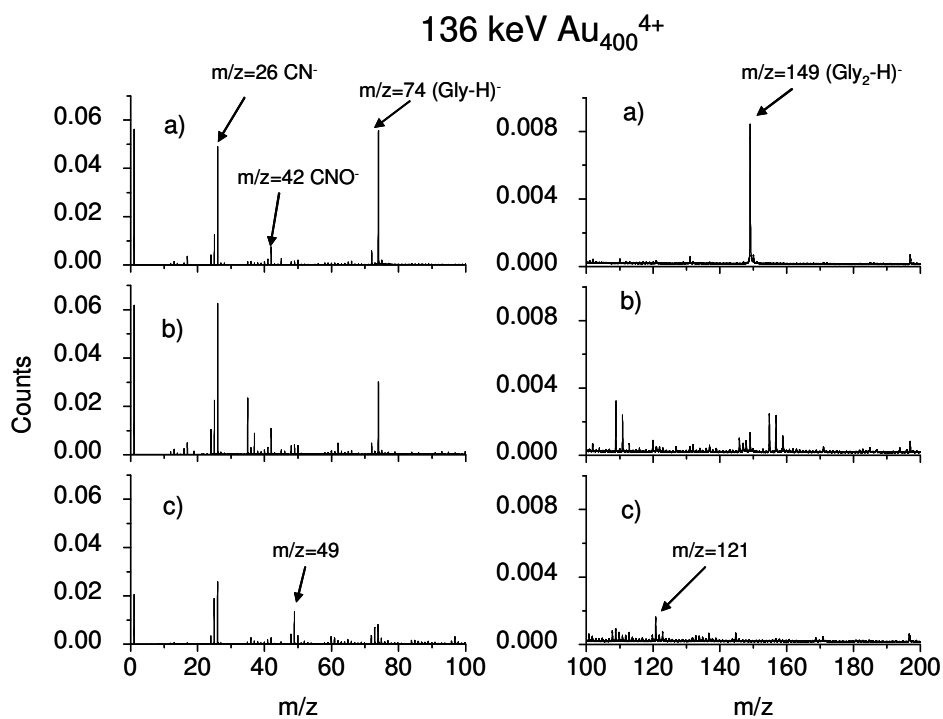
Figure 6-5 Negative ion mass spectra of vapor-deposited glycine analyzed with 136 keV Au_{400}^{4+}. a) pristine glycine, b) glycine after implanted with 5.0×10^{14} (1.6×10^{15} ions/cm^2) Na$^+$ ions at 100 eV, and c) glycine after implanted with 5.0×10^{14} (1.6×10^{15} ions/cm^2) Na$^+$ ions at 500 eV. Counts are normalized to the total number of events (~ 1×10^6 events).
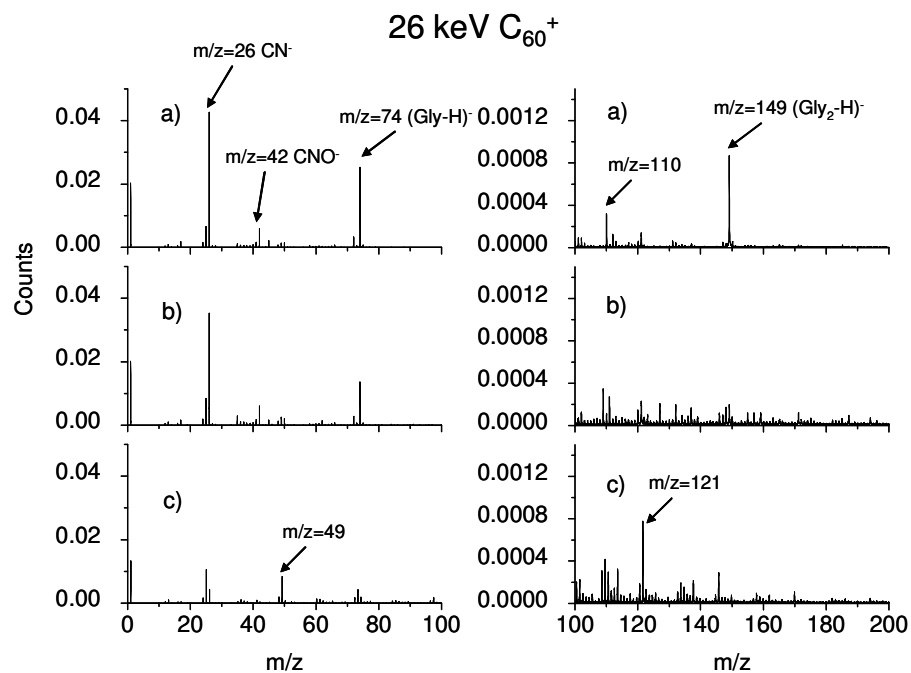
Figure 6-6 Negative ion mass spectra of vapor-deposited glycine analyzed with 26 keV C_{60}^+. a) pristine glycine, b) glycine after implanted with 5.0×10^{14} (1.6×10^{15} ions/cm^2) Na$^+$ ions at 100 eV, and c) glycine after implanted with 5.0×10^{14} (1.6×10^{15} ions/cm^2) Na$^+$ ions at 500 eV. Counts are normalized to the total number of events ($\sim 1\times10^6$ events).
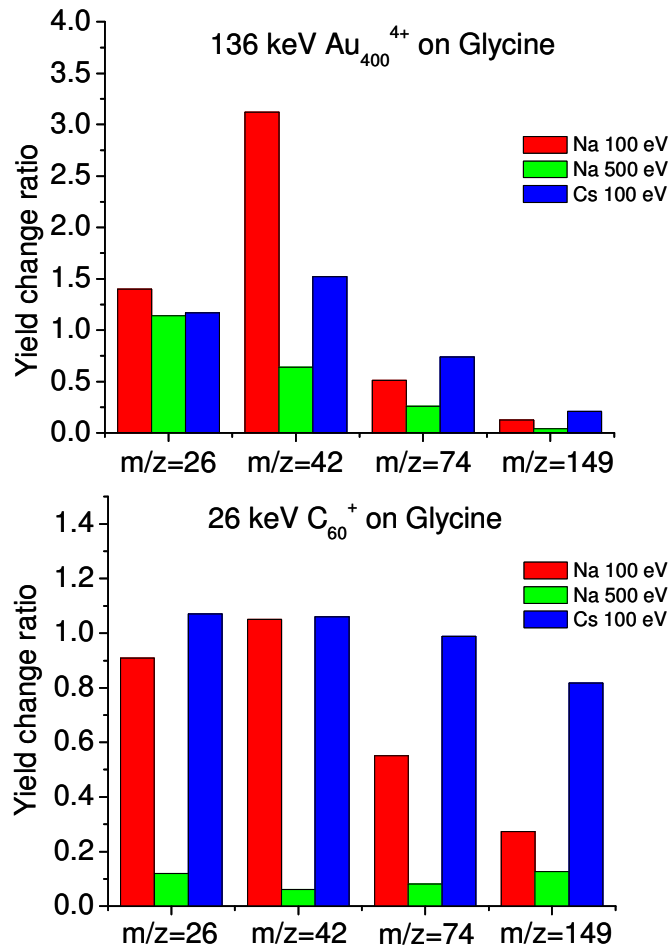
Figure 6-7 Comparison of the yield change ratios of selected SIs with Au_{400}^{4+} and C_{60}^{+} projectile impacts on glycine targets. Implantation dosage: 5.0×10^{14} $(1.6 \times 10^{15}$ ions/cm$^2)$.

damage compared with the Cs$^+$ beam at equal implantation energy.

91

CHAPTER VII

CONCLUSIONS

In this dissertation, we investigated some fundamental aspects of cluster SIMS:

- depth of SI emission.

- accuracy of the SI signal.

- volume of SI emission.

- effect of alkali metal ion implantation on the nature and abundance of SI emission.

We addressed the first three objectives with samples of controlled three dimensional structure, which were prepared using the layer-by-layer film assembling technique with PEI, PDDA, PSS, and clay nanoparticles.

The SI emission depth with 26 keV C_{60}^+ and 136 keV Au_{400}^{4+} projectile impacts was determined to be ~ 6-9 nm by monitoring SI signals from the PSS indicator layer. The diameter of the SI emission area is estimated to be ~ 15 nm by assuming a semispherical emission volume. Alternation of the compositions of the topmost layers results in the oscillation of the SI yields from the thin layer films. This phenomenon was observed with both small keV cluster projectiles ($CsICs^+$ and Au_3^+) as well as with the large cluster projectiles (C_{60}^+ and Au_{400}^{4+}). Comparing the various projectiles, the cluster species are most sensitive to the physico-chemical nature of the topmost layers of the surface.

The abundant co-emission from single impact/emission events with Au_{400}^{4+} projectile impacts allows to obtain chemical information from single emission volumes. The correlation coefficient, Q, can be used to evaluate the relationship between co-emitted SIs. Specifically, Q reveals submicron planar homogeneity of the films. In this case the Q values of co-emitted SIs from the clay and PSS layers showed a homogeneous distribution of the PSS layer and an uneven coverage of the

clay layers.

The high sensitivities of Au_{400}^{4+} and C_{60}^{+} projectile impacts can be applied to track accurately the presence of organics over a depth of a few nm with two caveats. The SI spectra obtained from C_{60}^{+} projectile impacts include a contribution from recoiled projectile constituents which preclude the accurate detection of organics via C^{-}, CH^{-}, C_2^{-} or C_3^{-}. The ionization and emission of small carbon cluster ions (C^{-} and CH^{-}) are enhanced in the presence of metal atoms in the expanding plume.

Future studies of SIMS analysis of the layer-by-layer thin films could incorporate proteins, DNA, and nanoparticles into the nanostructure. The proteins or DNA can be assembled as "preformed" anions by adjusting the pH values of their solutions. Such preformed anions can facilitate the emission of proteins and DNA as negative SIs. As mentioned in Chapter V, the ionization of low electron affinity species is enhanced by the interaction with the metal atoms in the expanding plume. Layer-by-layer thin films can be assembled to incorporate metal or metal oxide nanoparticle layers to enhance the SI yield of low electron affinity species. This principle can be used to assemble proteins and metal nanoparticles together to enhance the ionization of the biological molecules.

Investigation of the SI emission depth from the layer-by-layer thin films can be expanded to inorganic materials like SiO_2, metal and metal oxide nanoparticles. These inorganic nanoparticles have a discrete distribution on the surface due to the nature of their physical dimensions. One would expect a nanoparticle-to-nanoparticle interaction between the projectiles and the surface constituents when the massive cluster projectiles, which can also be considered as nanoparticles, are used to bombard these thin layer films. The nature and abundance of the SIs emitted will be altered in this nanoparticle-to-nanoparticle collision. Different SI emission depths are also expected.

Implantation studies with Na^{+} and Cs^{+} again allowed to test the depth of SI emission, which confirmed and amplified our understanding of the difference in the

depth of emission between molecular and fragment ions. The motivation for the implantation experiments was to assess the effect of lower surface work function on SI emission. It was observed that the implanted alkali metal ions destroy glycine molecules. The yield of glycine molecular ions decreases after implantation, while the yields of fragmentation/recombination ions (CN^- and CNO^-) show increase. The same implanted glycine sample analyzed with Au_{400}^{4+} projectile impacts show more molecular ion signal decrease than with C_{60}^+ projectile impacts. Such discrepancy suggests different mechanisms of SI emission with Au_{400}^{4+} and C_{60}^+ projectile impacts. The different behaviors of the yields of molecular and fragment ions suggest that they may come from different locations of the emission volume.

Beam-induced damage can be reduced by limiting the kinetic energy of the implantation beam. The ideal situation would be "soft-landing" of these alkali metal ions, i.e., with kinetic energy in the 1-20 eV range. Such low energy implantation requires modifications of the current implantation setup to precisely control the implantation energy and measure the implantation current. Ideally, this setup should be incorporated into the SIMS instrument to achieve *in situ* implantation and SIMS analysis. This will also reduce oxidation and contamination during transportation.

The SI yields under the experimental conditions described here range from less than 1% to more than 30%. Coincidental SI yields which are the key for nanovolume analysis are in the order of 0.1% to 1%. Future experiments should aim at increasing the SI and coincidental SI yields. This may be achieved by increasing the kinetic energy of the projectiles. However, one would ask how the molecular ion emission will evolve with increasing projectile energy. Which of the two trends will prevail at the level of an individual projectile impact: the increase in the volume of emission or an increase in the excitation energy imparted to the molecules?

The work presented here, while allowing to identify co-located species within 10-20 nm area, is non-imaging. Another direction for future experiments is to develop an imaging instrument. Recent experiments have shown that a chemical map

can be obtained by correlating the SIs with co-emitted secondary electrons through an emission electron microscope.

Last but not least, an issue which has not been addressed is that of the neutrals. Nothing is known about the sputtering yields with the projectiles used here. It is reasonable to assume that the high SI yields are not due to higher ionization efficiency but to a larger amount of ejecta per impact. Indeed, with 136 keV Au_{400}^{4+} projectile impacts, the ionization efficiency is estimated to be $\sim 2\times10^{-3}$ for small organic molecules. Prospects for laser postionization should be favorable recalling that MD simulations show the desorbed molecules carry little internal energy.

REFERENCES

[1]   A. Benninghoven, P. Bertrand, H.N. Migeon, H.W. Werner, Eds. Secondary Ion Mass Spectrometry-SIMS XII, Elsevier, Amsterdam, 2000.

[2]   N. Winograd, Anal. Chem. 77 (2005) 143A.

[3]   R.D. Harris, Ph.D. Dissertation, Texas A&M University, College Station, 1998.

[4]   D. Torgerson, R. Skowronsky, R. Macfarlane, Biochem. Biophys. Res. Commun. 60 (1974) 616.

[5]   P. Hakansson, I. Kamensky, B.U.R. Sundqvist, J. Fohlman, P. Peterson, C.J. McNeal, R.D. Macfarlane, J. Am. Chem. Soc. 104 (1982) 2948.

[6]   B.T. Chait, F.H. Field, Biochem. Biophys. Res. Commun. 134 (1986) 420.

[7]   G. P. Jonssoon, A.B. Hedin, P. Hakansson, B.U.R. Sundqvist, G.S. Save, P.F. Neilson, P. Roepstorff, K.E. Johansson, I. Kemensky, M.S.L. Lindberg, Anal. Chem. 58 (1986), 1084.

[8]   A. Hedin, P. Hakansson, M. Salehpour, B.U.R. Sundqvist, Phys. Rev. B 35 (1987) 7339.

[9]   I. Jardine, G. Scanlan, M. McNeil, P.J. Bernnan, Anal. Chem. 61 (1989) 416.

[10]   M. Caroff, C. Deprun, D. Karibian, L. Szabo, J. Biol. Chem. 266 (1991) 18543.

[11]   J.S. Lindsey, T. Chaudhary, B.T. Chait, Anal. Chem. 64 (1992) 2804.

[12]   M.J. Van Stipdonk, Ph.D. Dissertation, Texas A&M University, College Station TX, 1994.

[13]   A. Delcorte, Phys. Chem. Chem. Phys. 7 (2005) 3395.

[14]   W. Szymczak, K. Wittmack, Nucl. Instr. Meth. B 88 (1994) 149.

[15]   P.K. Pol, J.M. Fluit, J. Kistemaker, Physica 26 (1960) 1000.

[16]   F. Grønlund, W.J. Moore, J. Chem. Phys. 32 (1960) 1540.

[17]   H.H. Andersen, H.L. Bay, J. Appl. Phys. 45 (1974) 953.

[18]   H.H. Andersen, H.L. Bay, J. Appl. Phys. 46 (1975) 2416.

[19]   S.S. Johar, D.A. Thompson, Surf. Sci. 90 (1979) 319.

[20]   M.G. Blain, S. Della-Negra, J. Joret, Y. Le Beyec, E.A. Schweikert, Phys. Rev. Let. 63 (1989) 1625.

[21] A.D. Appelhans, J.E. Delmore, D.A. Dahl, Anal. Chem. 59 (1987) 1685.

[22] A.D. Appelhans, J.E. Delmore, Anal. Chem. 61 (1989) 1087.

[23] M. Benguerba, A. Brunelle, S. Della-Negra, J. Depauw, H. Joret, Y. Le Beyec, M.G. Blain, E.A. Schweikert, G. Ben Assayag, P. Sudraud, Nucl. Instrum. Meth. B 62 (1991) 8.

[24] K. Boussofiane-Baudin, G. Bolback, A. Brunelle, S. Della-Negra, P. Hakansson, Y. Le Beyec, Nucl. Instrum. Meth. B 88 (1994) 160.

[25] W. Szymczak, K. Wittmaack, NATO ASI Series B: Physics 269 (1991) 123.

[26] M.J. Van Stipdonk, R.D. Harris, E.A. Schweikert, Rap. Comm. Mass Spectrom. 10 (1996) 1987.

[27] M.J. Van Stipdonk, V. Santiago, E.A. Schweikert, J. Mass Spectrom. 34 (1999) 55.

[28] C.W. Diehnelt, M.J. Van Stipdonk, E.A. Schweikert, Int. J. Mass Spectrom. 207 (2001) 111.

[29] S.C.C. Wong, R. Hill, P. Blenkinsopp, N.P. Lockyer, D.E. Weibel, J.C. Vickerman, Appl. Surf. Sci. 203-204 (2003) 219.

[30] D. Weibel, S. Wong, N. Lockyer, P. Blenkinsopp, R. Hill, J.C. Vickerman, Anal. Chem. 75 (2003) 1754.

[31] C. Szakal, S. Sun, A. Wucher, N. Winograd, Appl. Surf. Sci. 231-232 (2004) 183.

[32] A.G. Sostarecz, S. Sun, C. Szakal, A. Wucher, N. Winograd, Appl. Surf. Sci. 231-232 (2004) 1179.

[33] A.G. Sostarecz, C.M. McQuaw, A. Wucher, N. Winograd, Anal. Chem. 76 (2004) 6651.

[34] S. Sun, A. Wucher, C. Szakal, N. Winograd, Appl. Phy. Lett. 84 (2004) 5177.

[35] A. Wucher, S. Sun, C. Szakal, N. Winograd, Anal. Chem. 76 (2004) 7234.

[36] A. Wucher, S. Sun, C. Szakal, N. Winograd, Appl. Surf. Sci. 231-232 (2004) 68.

[37] J. Cheng, N. Winograd, Anal. Chem. 77 (2005) 3651.

[38] J. Xu, C.W. Szakal, S.E. Martin, B.R. Peterson, A. Wucher, N. Winograd, J. Am. Chem. Soc. 126 (2004) 3902.

[39] J. Xu, S. Ostrowski, C.W. Szakal, A.G. Ewing, N. Winograd, Appl. Surf. Sci. 231-232 (2004) 159.

[40] S. Parry, N. Winograd, Anal. Chem. 77 (2005) 7950.

[41] J.E. Locklear, C. Guillermier, S.V. Verkhoturov, E.A. Schweikert, Appl. Surf. Sci. 252 (2006) 6624.

[42] J.F. Mahoney, J. Perel, T.D. Lee, P.A. Martino, P. William, J. Am. Soc. Mass Spectrom. 3 (1992) 311.

[43] J.F. Mahoney, E.A. Parilis, T.D. Lee, Nucl. Instrum. Meth. B 88 (1994) 154.

[44] R.A. Zubarev, I.S. Bitensky, P.A. Demirev, B.U.R. Sundqvist, Nucl. Instrum. Meth. B 88 (1994) 143.

[45] I. Yamada, Nucl. Instrum. Meth. B 112 (1996) 242.

[46] S. Bouneau, S. Della-Negra, J. Depauw, D. Jacquet, Y. Le Beyec, J.P. Mouffron, A. Novikov, M. Pautrat, Nucl. Instrum. Meth. B 225 (2004) 579.

[47] A. Tempez, J.A. Schultz, S. Della-Negra, J. Depauw, D. Jacquet, A. Novikov, Y. Le Beyec, M. Pautrat, M. Caroff, M. Ugarov, H Bensaoula, M. Gonin, K. Fufrer, A. Woods, Rap. Comm. Mass Spectrom. 18 (2004) 371.

[48] R.D. Rickman, S.V. Verkhoturov, G.J. Hager, E.A. Schweikert, Int. J. Mass Spectrom. 245 (2005) 48.

[49] A. Novikov, M. Caroff, S. Della-Negra, J. Depauw, M. Fallavier, Y. Le Beyec, M. Pautrat, J.A. Schultz, A. Tempez, A.S. Woods, Rap. Comm. Mass Spectrom. 19 (2005) 1851.

[50] G.J. Hager, C. Guillermier, S.V. Verkhoturov, E.A. Schweikert, Appl. Surf. Sci. 252 (2006) 6558.

[51] S.V. Verkhoturov, R.D. Rickman, C. Guillermier, G.J. Hager, J.E. Locklear, E.A. Schweikert, Appl. Surf. Sci. 252 (2006) 6490.

[52] A. Aoki, T. Seki, J. Matsuo, Z. Insepov, I. Yamada, Mat. Chem. Phys. 54 (1998) 139.

[53] M.F. Russo, B.J. Garrison, Anal. Chem. 78 (2006) 7206.

[54] B. Czwewinski, A. Delcorte, B.J. Garrison, R. Samson, N. Winograd, Z. Postawa, Appl. Surf. Sci. 252 (2006) 6419.

[55] C. Szakal, J. Kozole, M.F. Russo, B.J. Garrison, N. Winograd, Phys. Rev. Lett.

96 (2006) 216104.

[56] K.D. Krantzman, D.B. Kingsbury, B.J. Garrison, Nucl. Instrum. Meth. B 255 (2007) 238.

[57] A. Delcorte, B.J. Garrison, Nucl. Instrum. Meth. B 255 (2007) 223.

[58] C. Anders, H. Kirihata, Y. Yamaguchi, H.M. Urbassek, Nucl. Instrum. Meth. B 255 (2007) 247.

[59] C. Anders, H.M. Urbassek, Nucl. Instrum. Meth. B 228 (2005) 57.

[60] A. Delcorte, P. Bertrand, X. Arys, A. Jonas, E. Wischerhoff, B. Mayer, A. Laschewsky, Surf. Sci. 366 (1996) 149.

[61] D. Stapel, O. Brox, A. Benninghoven, Appl. Surf. Sci. 140 (1999) 156.

[62] C. Szakal, J. Kozole, N. Winograd, Appl. Surf. Sci. 252, (2006) 6526.

[63] K. Wittmaack, Surf. Sci. 126 (1983) 573.

[64] A. Hohlfeld, M. Sunjic, K. Horn, J. Vac. Sci. Technol. A 5 (1987) 679.

[65] D. Heskett, T. Maeda, A.J. Smith, W.R. Graham, N.J. DiNardo, E.W. Plummer, J. Vac. Sci. Technol. B 7 (1989) 915.

[66] P. Soukiassian, L. Spiess, K.M. Schirm, P.S. Mangat, J.A. Kubby, S.P. Tang, A.J. Freeman, J. Vac. Sci. Technol. B 11 (1993) 1431.

[67] B. Kierren, D. Paget, J. Vac. Sci. Technol. A 15 (1997) 2074.

[68] H. Yamazaki, S. Nakamura, Phys. Rev. B 59 (1999) 12298.

[69] T. Matsunaga, S. Yoshikawa, K. Tsukamoto, Surf. Sci. 515 (2002) 390.

[70] P.A.W. van der Heide, F.V. Azzarello, Surf. Sci. 531 (2003) L369.

[71] P.A.W. van der Heide, Appl. Surf. Sci. 231-232 (2004) 97.

[72] J. Brison, T. Conard, W. Vandervorst, L. Houssiau, Appl. Surf. Sci. 231-232 (2004) 749.

[73] B. Saha, P. Chakraborty, Nucl. Instru. Meth. B 258 (2007) 218.

[74] P. Philipp, T. Wirtz, H.N. Migeon, H. Scherrer, Int. J. Mass Spectrom. 264 (2007) 70.

[75] P. Hallegot, R. Peteranderl, C. Lechene, J. Investig. Dermatol. 122 (2004) 381.

[76] G. McMahon, B.J. Glassner, C.P. Lechene, Appl. Surf. Sci. 252 (2006) 6895.

[77] C. Lechene, F. Hillion, G. McMahon, D. Benson, A. Kleinfeld, J.P. Kampf, D. Distel, Y. Luyten, J. Bonventre, D. Hentschel, K. Park, S. Ito, M. Schwartz, G.

Benichou, G. Slodzian, J. Biol. 5 (2006) 20.

[78] T. Wirtz, H.N. Migeon, Appl. Sur. Sci. 231-232 (2004) 940.

[79] P. Philipp, T. Wirtz, H.N. Migeon, H. Scherrer, Appl. Surf. Sci. 231-232 (2004) 754.

[80] P. Philipp, T. Wirtz, H.N. Migeon, H. Scherrer, Int. J. Mass Spectrom. 253 (2006) 71.

[81] P. Philipp, T. Wirtz, H.N. Migeon, H. Scherrer, Int. J. Mass Spectrom. 261 (2007) 91.

[82] R.D. MacFarlane, Anal. Chem. 55 (1983) 1247A.

[83] B.U.R. Sundqvist, R.D. MacFarlane, Mass Spectrom. Rev. 4 (1985) 421.

[84] J.H. Moore, C.C. Davis, M.A. Coplan, Building Scientific Apparatus: A Practical Guide to Design and Construction 2nd Ed., Perseus Books, Cambridge, Massachusetts 1991.

[85] R.D. Rickman, Ph.D. Dissertation, Texas A&M University, College Station, TX, 2004.

[86] G.J. Hager, Ph.D. Dissertation, Texas A&M University, College Station ,TX, 2007.

[87] M. Guilhaus, J. Mass Spectrom. 30 (1995) 1532.

[88] B.D. Cox, M.A. Park, R.G. Kaercher, E.A. Schweikert, Anal. Chem. 64 (1992) 843.

[89] J.L. Wiza, Nucl. Instr. Meth. 162 (1979) 587.

[90] I.S. Gilmore, M.P. Seah, Int. J. Mass Spectrom. 202 (2000) 217.

[91] E.F. da Silveira, S.B. Duarte, E.A. Schweikert, Surf. Sci. 408 (1998) 28.

[92] R.D. Rickman, S.V. Verkhoturov, E.S. Parilis, E.A. Schweikert, Phys. Rev. Lett. 92 (2004) 047601.

[93] Z. Postawa, C. Bartlomiej, M. Szewczyk, E.J. Smiley, N. Winograd, B.J. Garrison, Anal. Chem. 75 (2003) 4402.

[94] Z. Postawa, B. Czerwinski, N. Winograd, B.J. Garrison, J. Phys. Chem. B 109 (2005) 11973.

[95] I.A. Wojciechowski, B.J. Garrison, J. Phys. Chem. A 110 (2006) 1389.

[96] M.A. Park, K.A. Gibson, L. Quinones, E.A. Schweikert, Science 248 (1990)

988.

[97] M.J. Van Stipdonk, E.A. Schweikert, M.A. Park, J. Mass. Spectrom. 32 (1997) 1151.

[98] S.V. Verkhoturov, E.A. Schweikert, N.M. Rizkalla, Langmuir 18 (2002) 8836.

[99] G. Decher, J. Schmitt, Thin Solid Films 210-211 (1990) 831.

[100] G. Decher, Science 277 (1997) 1232.

[101] Y. Lvov, G. Decher, H. Mohwald, Langmuir 9 (1993) 481.

[102] Y. Lvov, K. Ariga, I. Ichinose, T. Kunitake, Thin Solid Films 284-285 (1996) 797.

[103] A. Mamedov, J. Ostrander, F. Aliev, N.A. Kotov, Langmuir 16 (2000) 3941.

[104] J.B. Schlenoff, S.T. Dubas, Macromolecules 34 (2001) 592.

[105] D.W. Kim, A. Blumstein, S.K. Tripathy, Chem. Mater. 13 (2001) 1916.

[106] Y. Zhou, Z. Li, N. Hu, Y. Zeng, J.F. Rusling, Langmuir 18 (2002) 8573.

[107] D.W. Kim, H.-S. Choi, C. Lee, A. Blumstein, K. Kang, Electrochimica Acta 50 (2004) 659.

[108] A. Izquierdo, S.S. Ono, J.C. Voegel, P. Schaaf, G. Decher, Langmuir 21 (2005) 7558.

[109] Y. Lvov, K. Ariga, I. Ichinose, T. Kunitake, Langmuir 12 (1996) 3038.

[110] R.D. English, M.J. Van Stipdonk, R.C. Sabapathy, R.M. Crooks, E.A. Schweikert, Anal. Chem. 72 (2000) 597.

[111] I. Moriguchi, J. H. Fendler, Chem. Mater. 10 (1998) 2205.

[112] T. Nakanishi, B. Ohtani, K. Uosaki, J. Phys. Chem. B 102 (1998) 1571.

[113] T. Sasaki, Y. Ebina, T. Tanaka, M. Harada, M. Watanabe, G. Decher, Chem. Mater. 13 (2001) 4661.

[114] R.D. Harris, M.J. Van Stipdonk, E.A. Schweikert, Int. J. Mass Spectrom. Ion Proc. 174 (1998) 167.

[115] G. Gillen, L. King, B. Freibaum, R. Lareau, J. Bennett, F. Chmara, J. Vac. Sci. Technol. A 19 (2001) 568.

[116] J.E. Locklear, S.V. Verkhoturov, E.A. Schweikert, Int. J. Mass Spectrom. 238 (2004) 59.

[117] S.R. Bryan, A.M. Belu, T. Hoshi, R. Oiwa, Appl. Surf. Sci. 231-232 (2004)

201.

[118] D. Touboul, F. Kollmer, E. Niehuis, A. Brunelle, O. Laprévote, J. Am. Soc. Mass Spectrom. 16 (2005), 1608.

[119] R.D. Rickman, S.V. Verkhoturov, E.A. Schweikert, Appl. Surf. Sci. 231-232 (2004) 54.

[120] L.A. Currie, Anal. Chem. 40 (1968) 586.

[121] K. Ariga, Y. Lvov, I. Ichinose, T. Kunitake, Appl. Clay Sci. 15 (1999) 137.

[122] Z. Li, S.V. Verkhoturov, E.A. Schweikert, Anal. Chem. 78 (2006) 7410.

[123] R. Holm, S. Storp, Surf. Interf. Anal. 2 (1980) 96.

[124] W. Harbich, in K.H. Meiwes-Broer (Ed.), Metal Clusters at Surfaces: Structure, Quantum Properties, Physical Chemistry, Springer, Berlin, 2000, pp. 123-125.

[125] C.W. Diehnelt, M.J. Van Stipdonk, E.A. Schweikert, Nucl. Instrum. Meth. B 142 (1998) 606.

[126] M.H. Shapiro, T.A. Tombrello, Phys. Rev. Lett. 68 (1992) 1613.

[127] A. Delcorte, S. Yunus, N. Wehbe, N. Nieuwjaer, C. Poleunis, A. Felten, L. Houssiau, J.J. Pireaux, P. Bertrand, Anal. Chem. 79 (2007) 3673.

[128] J.F. Ziegler, J.P. Biersack, U. Litmark, in: J.F. Ziegler (Ed.), Stopping Power and Ranges of Ions in Matter, Vol. 1, Pergamon, New York, 1985, pp. 321-350.

VITA

Name: Zhen Li

Address: c/o Professor Emile A. Schweikert

             Department of Chemistry

             Texas A&M University, College Station, TX 77843-3255

Email: lizhenchem@hotmail.com

Phone: 979-575-9641

Education: B.S. Chemistry, Beijing Normal University, 1999
M.S. Chemistry, Beijing Normal University, 2002
Ph.D. Chemistry, Texas A&M University, 2007